

Accepted Manuscript

South Atlantic Interbasin Exchanges of Mass, Heat, Salt and Anthropogenic Carbon

G.R. Evans, E.L. McDonagh, B.A. King, H.L. Bryden, D.C.E. Bakker, P.J. Brown, U. Schuster, K.G. Speer, S.M.A.C. van Heuven

PII: S0079-6611(15)30038-0

DOI: <http://dx.doi.org/10.1016/j.pocean.2016.11.005>

Reference: PROOCE 1754

To appear in: *Progress in Oceanography*

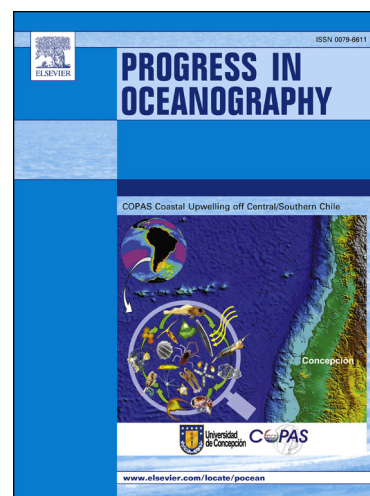
Received Date: 25 October 2015

Revised Date: 30 October 2016

Accepted Date: 16 November 2016

Please cite this article as: Evans, G.R., McDonagh, E.L., King, B.A., Bryden, H.L., Bakker, D.C.E., Brown, P.J., Schuster, U., Speer, K.G., van Heuven, S.M.A.C., South Atlantic Interbasin Exchanges of Mass, Heat, Salt and Anthropogenic Carbon, *Progress in Oceanography* (2016), doi: <http://dx.doi.org/10.1016/j.pocean.2016.11.005>

This is a PDF file of an unedited manuscript that has been accepted for publication. As a service to our customers we are providing this early version of the manuscript. The manuscript will undergo copyediting, typesetting, and review of the resulting proof before it is published in its final form. Please note that during the production process errors may be discovered which could affect the content, and all legal disclaimers that apply to the journal pertain.



South Atlantic Interbasin Exchanges of Mass, Heat, Salt and Anthropogenic Carbon

G. R. Evans^{1,2}, E. L. McDonagh³, B. A. King³, H. L. Bryden^{2,3}, D. C. E. Bakker⁴, P. J. Brown³, U. Schuster⁵, K. G. Speer⁶, S. M. A. C. van Heuven⁷

1. Met Office, FitzRoy Road, Exeter, UK
2. School of Ocean and Earth Science, National Oceanography Centre, University of Southampton, Southampton, UK
3. National Oceanography Centre, Southampton, UK
4. Centre for Ocean and Atmospheric Sciences, School of Environmental Sciences, University of East Anglia, Norwich Research Park, Norwich, UK
5. College of Life and Environmental Sciences, University of Exeter, Exeter, UK
6. Geophysical Fluid Dynamics Institute and Dept. of Earth, Ocean, and Atmospheric Sciences, Florida State University, Tallahassee, USA
7. Royal Netherlands Institute for Sea Research, 1790 AB Den Burg, The Netherlands

Abstract

The exchange of mass, heat, salt and anthropogenic carbon (C^{ant}) between the South Atlantic, south of 24°S , and adjacent ocean basins is estimated from hydrographic data obtained during 2008-2009 using an inverse method. Transports of anthropogenic carbon are calculated across the western (Drake Passage), eastern (30°E) and northern (24°S) boundaries. The freshwater overturning transport of 0.09 Sv is southward, consistent with an overturning circulation that exports freshwater from the North Atlantic, and consistent with a bistable Meridional Overturning Circulation (MOC), under conditions of excess freshwater perturbation. At 30°E , net eastward Antarctic Circumpolar Current (ACC) transport, south of the Subtropical Front, is compensated by a $15.9\pm 2.3\text{ Sv}$ westward flow along the Antarctic boundary. The region as a whole is a substantial sink for atmospheric anthropogenic carbon of $0.51\pm 0.37\text{ PgC yr}^{-1}$, of which $0.18\pm 0.12\text{ PgC yr}^{-1}$ accumulates

and is stored within the water column. At 24°S, a 20.2 Sv meridional overturning is associated with a $0.11 \text{ PgC yr}^{-1} \text{ C}^{\text{ant}}$ overturning. The remainder is transported into the Atlantic Ocean north of 24°S ($0.28 \pm 0.16 \text{ PgC yr}^{-1}$) and Indian sector of Southern Ocean ($1.12 \pm 0.43 \text{ PgC yr}^{-1}$), having been enhanced by inflow through Drake Passage ($1.07 \pm 0.44 \text{ PgC yr}^{-1}$). This underlines the importance of the South Atlantic as a crucial element of the anthropogenic carbon sink in the global oceans.

1 Introduction

At the confluence of the southward-flowing deep water from the northern North Atlantic Ocean and the eastward-flowing Antarctic Circumpolar Current (ACC), the South Atlantic sector of the Southern Ocean is a key component of the global meridional overturning circulation (MOC; Marshall and Speer 2012). The critical role of the South Atlantic was recognised by Rintoul (1991), who quantified the basic heat and freshwater exchange associated with balancing deep-water formation in the North Atlantic with Intermediate Water and Bottom Water formation in the Southern Ocean. Overturning within the South Atlantic is critical for the ventilation of older water masses facilitating uptake and storage of anthropogenic carbon (C^{ant}) (Iudicone et al., 2011; Sallée et al., 2012). Bottom Water formation; in particular, provides a mechanism for injection of C^{ant} into the deep ocean (Brown et al., 2015; Vázquez-Rodríguez et al., 2009).

This paper focuses on the South Atlantic sector of the Southern Ocean south of 24°S from Drake Passage to 30°E. The ACC crosses this region and, together with the Agulhas Current, links the Pacific and Indian Ocean sectors of this region. The ACC transport is concentrated into fronts (Subantarctic Front, SAF; Polar Front, PF; Southern ACC Front, SACCF), which preferentially carry different water classes and properties across the region (see Figure 1). Drake Passage is the narrow entry point for the ACC into the Atlantic sector, after which, the Subantarctic Front protrudes northwards into the Argentine Basin. This widens the meridional extent of the ACC, and separates the warmer subtropical waters to the north from colder, Antarctic and Subantarctic water to the south (Belkin and Gordon, 1996; Orsi et al., 1995).

North of the ACC in the Atlantic sector, the poleward-flowing Brazil Current (BC) lies within the upper 300-600 dbar (Bryden et al., 2011; Peterson and Stramma, 1991). Fully formed north of the Vitoria-Trinidad Seamounts at $\sim 20^{\circ}\text{S}$ (marked in Figure 1), it intensifies southwards on the order of 5% per 100 km (Gordon and Greengrove, 1986) with transport estimates at 24°S ranging between 4.1 Sv and 13.2 Sv (Bryden et al., 2011; Evans et al., 1983; Evans and Signorini, 1985; Garfield, 1990; Signorini, 1978; Stramma, 1989; Zemba, 1991). At the eastern South Atlantic boundary within the Cape Basin, the South Atlantic Current (SAC) feeds the northward flowing Benguela Current. Previous transport estimates are of 6 Sv for the South Atlantic Current and 28 Sv for the Benguela Current, respectively (Garzoli and Gordon, 1996; Mercier et al., 2003; Smythe-Wright et al., 1998; Stramma and Peterson, 1990). The Benguela Current is also fed by the residual westward flow into the South Atlantic from the Agulhas system, commonly termed Agulhas leakage. The majority of the Agulhas Current flows along the East African continent, and is retroflected at $16\text{-}20^{\circ}\text{E}$ (Lutjeharms and Van Ballegooyen, 1988) as the eastward flowing Agulhas Return Current, closing the subtropical gyre of the South Indian Ocean (Dencausse et al., 2010; Lutjeharms and Van Ballegooyen, 1988; Matano et al., 1998).

South of the ACC in the Atlantic sector, previous studies (e.g. Meredith, 2013) have suggested that the Weddell Sea contributes to about 40% of the global formation of Antarctic Bottom Water (AABW). Westward inflow along the Antarctic shelf into the Weddell Sea is partially comprised of recently formed Cape Darnley Bottom Water (CDBW; Ohshima et al. 2013) and older AABW varieties from farther east. CDBW contributes $\sim 13\text{-}30\%$ to global AABW production (Ohshima et al., 2013). Within the Weddell Sea, local ventilation and interaction with the Filchner-Ronne (Whitworth et al., 1998) and Larsen (Fahrbach et al., 1995; Weppernig et al., 1996) ice shelves contributes to further AABW formation, carrying C^{ant} into the deep ocean (Huhn et al., 2013; van Heuven et al., 2011). Some of this AABW recirculates within the eastward flowing northern limb of the Weddell Gyre, whilst the remainder escapes either into the western South Atlantic basin through narrow deep water pathways (e.g. Gordon et al., 2010, Jullion et al., 2014), by South Scotia Ridge overflow (Jullion et al., 2014; Locarnini et al.,

1993; Naveira Garabato et al., 2002a), or into the eastern South Atlantic basin with 8 ± 2 Sv of AABW in total exported from the Weddell Gyre (Jullion et al., 2014). At the Argentine Basin to Brazil Basin transition, northward AABW flow is restricted to key topographical features (Figure 1): Vema Channel (25-50 km wide, sill depth ~ 4600 m; Johnson and Biscaye (1976)) and Hunter Channel (200 km wide, sill depth ~ 4200 m; Speer et al. (1992); Zenk et al. (1999)). Bottom water warming between the Weddell Sea and 24°S alters the typical bottom water definition from $\theta \leq 0^\circ\text{C}$ to $\theta \leq 2^\circ\text{C}$. Bottom water transports for $\theta < 2^\circ\text{C}$ are 4.0 ± 1.2 Sv at Vema Channel (Hogg et al., 1999), and 2.92 ± 1.24 Sv at Hunter Channel (Zenk et al., 1999).

The MOC, ACC, Agulhas system and Weddell Gyre are all major contributors to the global large-scale ocean circulation, and therefore an understanding of their contribution to interbasin fluxes is key for interpreting large-scale changes in volume, heat or freshwater transports, and identifying linkages to broader changes in the Earth's climate. Similarly interbasin fluxes of anthropogenic carbon (C^{ant}) provide an opportunity to assess the South Atlantic's capacity to uptake and store anthropogenic carbon on decadal-centennial timescales, in order to improve understanding of its responses to future atmospheric CO_2 changes. Here, C^{ant} is estimated using the ΔC^* method following Gruber et al. (1996), as described in section 2.1 and in further detail in Evans (2013).

This paper uses a set of recent WOCE sections at the boundary of the South Atlantic Ocean to update interbasin flux estimates of mass, heat and salt in comparison to earlier studies (e.g. Rintoul, 1991), and to provide estimates of the interbasin flux of anthropogenic carbon (C^{ant}). This paper is structured as follows: Section 2 describes the data used. Section 3 outlines the inverse box methodology, as applied in this study. The solution of the inverse box model is discussed in Section 4 in terms of geostrophic and Ekman velocity fields, diapycnal mixing and air sea fluxes of heat and freshwater as well as the transports of anthropogenic carbon at the South Atlantic boundary. The major findings are described in Section 5.

2 Data and Data Processing

Hydrographic sections in Drake Passage (a repeat of World Ocean Circulation Experiment (WOCE) section A21) in 2009, Africa to Antarctica along 30°E (repeat of WOCE I6S) in 2008 and South America to Africa along 24°S in 2009 provide the data for analysis. The Drake Passage and 24°S sections were occupied on board the research vessel James Cook (King, 2010; McDonagh, 2009), with data stored within the British Oceanographic Data Centre data archives, whilst the Africa to Antarctica occupation was on board the Roger Revelle, with data stored by the CLIVAR (Climate Variability and Predictability) and Carbon Hydrographic Data Office (CCHDO) (Speer and Dittmar, 2008; Wanninkhof et al., 2009).

Dissolved Inorganic Carbon (DIC) and Total Alkalinity were determined by coulometry (Johnson et al. 1985, 1987, 1993; Johnson and Wallace 1992) and potentiometric titration (Johnson et al., 1987; Dickson et al. 2003, 2007; Mintrop 2004), respectively. DIC and Total Alkalinity were calibrated using Certified Reference Materials (CRM) (and gaseous CO₂ loops for DIC along 30°E) to yield measurements with an accuracy of $\sim\pm 2-3 \mu\text{mol kg}^{-1}$ (Speer and Dittmar, 2008; McDonagh, 2009; King, 2010; Schuster et al. 2013, 2014). Oxygen was measured using Winkler titration (Culberson et al., 1991; Culberson and Huang, 1987), whilst nitrate, phosphate and silicate measurements follow the processes described in Gordon et al. (1993) and Kirkwood (1996). Estimated accuracies according to CARINA methodology are oxygen (1%) and nutrients (2%) (Key et al., 2010). All salinities used are on the PSS-78 scale (Fofonoff and Millard, 1983).

Hydrographic properties were recorded using a conductivity-temperature-depth (CTD) profiler in 2 dbar intervals, to enable geostrophic transport estimates. Geostrophic velocity within the 'bottom triangle' is set by nearest neighbour extrapolation to the deepest common level for each station pair. DIC, nutrient and alkalinity measurements are recorded for a maximum of 24, or 36 discrete depths per station for Drake Passage and 24°S, and 30°E, respectively. Potential temperature (θ), salinity and oxygen are linearly interpolated onto a 20 dbar vertical grid along the sections. Correction factors are applied, as recommended by the GLODAP (Global Ocean Data Analysis Project) and CARINA (Carbon in Atlantic Ocean) projects, listed in Table 1, to eliminate systematic

measurement biases (see Gouretski and Jancke, 2000; Hoppema et al., 2009; Key et al., 2010, 2004; Lauvset et al., 2016; Olsen et al., 2016; Tanhua et al., 2010; Wanninkhof et al., 2003).

The geographical locations of the sections are displayed in Figure 1. ACC fronts along Drake Passage are determined as a distinct transition in θ -S space between θ -S hydrographic station profiles. Each transition represents an ACC front separating each frontal zone, and follows the Cunningham et al. (2003) analysis. Across 30°E, thermohaline frontal definitions from Orsi et al. (1995) and Belkin and Gordon (1996) are applied.

2.1 Anthropogenic Carbon Calculation

Anthropogenic carbon is estimated here using the ΔC^* method, whereby biological effects, a pre-industrial background signal (based on ocean-atmospheric equilibrium (C^{eqm}) (Brewer, 1978; Chen and Millero, 1979) and an estimate of ocean-atmosphere disequilibrium (C^{diseq}) (Gruber et al., 1996) are removed from the modern inorganic carbon signal. C^{eqm} is calculated based on pre-industrial fugacity ($f\text{CO}_2 = 280 \mu\text{atm}$), and present day potential temperature, salinity, silicate and phosphate using “CO2SYS.m” (Lewis and Wallace, 1998). C^{diseq} is represented using the linearised parameterisations for specified potential temperature intervals from Pardo et al. (2011) (Indian/Pacific Ocean) and Vázquez-Rodríguez et al. (2012) (Atlantic Ocean) and an Optimum Multiparameter Analysis (OMP) technique (Karstensen and Tomczak, 1998; Sabine et al., 2002) below the 5°C isotherm. C^{eqm} and C^{diseq} utilise the potential total alkalinity parameterisation from Vázquez-Rodríguez et al. (2012), and the conversion from potential total alkalinity to total preformed alkalinity following Brewer et al. (1975) and Fraga and Álvarez-Salgado (2005). The uncertainty of C^{ant} estimates calculated using this method is up to $\sim 6 \mu\text{mol kg}^{-1}$ (Sabine et al., 1999). For visualisation and comparison in Section 4.3.1, a two-dimensional distribution in neutral density:geopotential height or neutral density:longitude space of C^{ant} is generated by least squares fitting using a ± 2 station and $\pm 0.04 \gamma^n$ grid box centred at each CTD grid point. The geopotential height (φ) field is calculated from the geopotential height anomaly at 500 dbar relative to 1500 dbar for

neighbouring stations. For transport calculations in Section 4.3.2, a two-dimensional distribution in pressure:latitude or pressure:longitude space of C^{ant} is generated by least squares fitting using a ± 2 station and ± 80 dbar grid box centred at each CTD grid point. Full details of the calculation of C^{ant} are found in Evans (2013).

2.1.1 Anthropogenic carbon storage

Two independent methods are used to calculate the rate of accumulation of anthropogenic carbon within the South Atlantic water column. The first is based on the assumption of a transient steady state relationship between surface carbon changes and at depth, following the methodology of Holfort et al. (1998) and Álvarez et al. (2003). This approach has been indicated to be broadly consistent with Green's Function and inverse approaches (Khatiwala et al., 2013). Secondly we use results of the Time Series Residual (TSR) approach (van Heuven et al., 2011; van Heuven, 2013), where a residual DIC is calculated from the difference between measured DIC and synthetic DIC values constructed from a multivariate linear regression of all available data points. The time trend of that residual DIC is interpreted as equivalent to the time trend of C^{ant} . The TSR-based C^{ant} storage estimate (provided by van Heuven, S. (2016), manuscript in preparation) uses all historical carbon data from 1972-2012 from the GLODAPv2 data product (Olsen et al., 2016) as well as the climatologies produced therewith (Lauvset et al., 2016).

2.1.1.1 Mean penetration depth (MPD)

In general terms, the build-up of carbon within any ocean basin is given by the difference between box boundary transports and atmosphere – sea-surface exchange, whilst assuming a negligible effect for a number of compensatory processes (following Álvarez et al. (2003)): riverine input (Holfort and Siedler, 2001; Jacobson et al., 2007), meltwater input (Rignot et al., 2008), net organic carbon production and sediment burial (Rosón et al., 2003; Sarmiento et al., 1995), and calcium carbonate dissolution and burial (Stoll et al., 1996). Other transient terms related to seasonal or biological variability at the box boundary are assumed as negligible for the basin-wide C^{ant} storage estimate. As diapycnal and air-sea induced diapycnal transfer do not add or remove C^{ant} from the full depth C^{ant}

budget, the inclusion of only geostrophic and Ekman effects therefore create the following equation:

$$C^{\text{ant}} \text{ Storage} = F_{\text{air-sea}} + T_N + T_W + T_E \quad (1)$$

with the average air-sea C^{ant} flux being $F_{\text{air-sea}}$ and T_N , T_W and T_E being C^{ant} transports across the northern, western and eastern boundaries of the South Atlantic Ocean sector (Figure 1). For C^{ant} , storage is represented by the temporal increase of C^{ant} throughout the water column, or mathematically by:

$$C^{\text{ant}} \text{ Storage rate} = \frac{d \int C_z^{\text{ant}} dz}{dt} \quad (2)$$

where t is time and $\int C_z^{\text{ant}} dz$ is the accumulation of anthropogenic CO_2 at each depth level z yielding a storage rate with units of $\text{mol m}^{-2} \text{ yr}^{-1}$ (Álvarez et al., 2003). An approximation for the magnitude of the anthropogenic CO_2 storage is calculated from the mean penetration depth (MPD) from Broecker et al., (1979):

$$\text{MPD} = \frac{\int C_z^{\text{ant}} dz}{C_{\text{ml}}^{\text{ant}}} \quad (3)$$

where C_z^{ant} and $C_{\text{ml}}^{\text{ant}}$ are anthropogenic CO_2 estimates at depth, z , and within the mixed layer, respectively. MPD is therefore the C^{ant} column inventory divided by C^{ant} from the mixed layer, and always yields a depth which is shallower than the actual depth to which the tracer penetrates (Peacock, 2004). Combining equation 2 and 3 gives an estimate of the anthropogenic CO_2 storage rate:

$$C^{\text{ant}} \text{ Storage rate} = \frac{d \int C_z^{\text{ant}} dz}{dt} = \text{MPD} \times \frac{dC_{\text{ml}}^{\text{ant}}}{dt} \quad (4)$$

This assumes that the vertical profile of C^{ant} is constant in shape and scale depth with time following the transient steady-state assumption of Gammon et al. (1982). This prescribes that a conservative tracer propagating into an ocean with steady circulation, but forced by an exponentially-increasing atmospheric boundary source function, will reach a transient steady state with constant shape. Mixed layer increases in C^{ant} are then assumed to increase proportionally with tracer concentrations at all depths (Tanhua et al., 2007). C^{ant} is thought to have passed into transient steady-state, given the length of its atmospheric history (>200 years). The MPD assumptions are most problematic in regions of significant deep water ventilation, where the assumption of a constant vertical C^{ant} profile to the ocean bottom may be false. In this study, recently ventilated deep waters, in

the form of AABW along Drake Passage and 30°E sections, still maintain low C^{ant} . This helps to validate the usage of an MPD-based C^{ant} storage rate estimate in this instance, however, this methodology contributes to a relatively large uncertainty in the result.

The $\Delta C_{\text{ml}}^{\text{ant}}$ is calculated by determining the rate of change in mean C^{ant} within the mixed layer between occupations. In this study, $\Delta C_{\text{ml}}^{\text{ant}}$ is computed using historical hydrographic occupations of Drake Passage (Meteor: 1990) and 30°E (Marion Dufresne: 1996) with further details in Evans (2013). Along the 24°S transect, $\Delta C_{\text{ml}}^{\text{ant}}$ is calculated based on overlapping stations from meridional hydrographic occupations A13, A14 (Mercier and Arhan, 1995), A15 (Smethie and Weatherly, 1994), A16 (Talley et al., 1989) and A17 (Mémery, 1994) within the South Atlantic. This constitutes all historical data for the region available within GLODAPv2 (see Appendix B for details). The small sample of repeat DIC measurements at the northern boundary increases storage uncertainty. Storage rate is re-written as:

$$\text{Storage rate} = \text{MPD} \times \Delta C_{\text{ml}}^{\text{ant}} \times \rho_{\text{ml}} \quad (5)$$

where ρ_{ml} is the in-situ density within the mixed layer yielding storage rate with units of $\text{mol m}^{-2} \text{yr}^{-1}$.

2.1.1.2 Time Series Residual (TSR)

TSR-based C^{ant} storage estimates rely upon assumptions that (i) the relationship between DIC and the independent variables in the regression is linear, that (ii) bias and noise within the sampling is considered negligible (or average out for the large dataset employed) and that (iii) real changes in one or more independent variable is associated with changes in one or more of the other independent variables (van Heuven, 2013). The time trend in C^{ant} is expected to depend upon the ventilation age of the water mass, with AOU used as a proxy for ventilation age. For a particular water mass, i , the time trend of C^{ant} is represented by the linear regression of:

$$\frac{dC_i^{\text{ant}}}{dt} = a_i + \Delta \text{AOU} \cdot b_i \quad (6)$$

Where ΔAOU is the difference between the AOU of the sample and the mean AOU in the water mass core (van Heuven, 2013). The contribution of a water mass to a given

sample is determined using Optimum Multiparameter analysis (OMP) (Karstensen and Tomczak, 1998; Sabine et al., 2002; van Heuven, 2013). The C^{ant} storage for the South Atlantic basin is thus estimated by the inclusion of a gridbox mass following:

$$\frac{d^{\text{INV}}C_i^{\text{ant}}}{dt} = \sum_{i=1}^j x_i \cdot (a_i + \Delta\text{AOU} \cdot b_i) \cdot \text{GBM} \quad (7)$$

Where x_i is the fractional contribution of water mass i to the inventory, and GBM represents the mass of a grid box surrounding each grid point, as described in van Heuven, (2013). The resulting inventory ($d^{\text{INV}}C_i^{\text{ant}}/dt$) can be expressed in units of PgC yr⁻¹.

3 Box Inverse analysis

3.1 Setup

The box inverse framework combines initial estimates of the circulation on each of the three hydrographic sections (Section 3.2) with constraints on the large-scale circulation, convergence of properties in the box, mixing and air-sea fluxes (Section 3.3). This generates an estimate of the circulation, the solution that is consistent across all three sections and the enclosed region (Section 3.4). The hydrographic sections used here (Figure 1) were made in February and early April, however, in either 2008 or 2009. The lack of synopticity of the data increases the uncertainty; however, this is partially accounted for by the choice of constraints to avoid a synoptic bias. This solution for this inverse box model is therefore most representative of South Atlantic circulation during austral summer.

The setup and method used is summarised here and detailed in Wunsch (1996). The inverse box model with the additional inclusion of noise vector ε to account for errors (Evans, 2013), is represented by:

$$\mathbf{E}\mathbf{x} + \varepsilon = \mathbf{y} \quad (8)$$

\mathbf{E} is an $m \times n$ matrix, \mathbf{x} is an $m \times 1$ vector of unknowns and \mathbf{y} is an $m \times 1$ vector of the imbalance between the initial field and the constraints. The coefficients in \mathbf{E} represent the geometry of the section. Each row of \mathbf{E} represents a constraint on the system. Each

column of \mathbf{E} represents an unknown. In this study, the system has 340 unknowns and 73 constraints. The unknowns are those elements of the system that can be adjusted in order to satisfy the constraints. The inverse model solves for 217 depth-independent \mathbf{x} velocities, one from each pair of adjacent hydrographic stations on each section. In addition, a single unknown represents the correction to the Ekman transport on the 24°S section, whilst 60 unknowns represent the mixing of volume, temperature and salinity between density layers within the box and another 62 unknowns represent the transformation between layers driven by air-sea interaction.

3.2 Initial Field

Flow across the sections is assumed to be geostrophic with an additional surface Ekman transport across 24°S. An initial reference level and geostrophic field is constructed for each section (Table 2) based on historical analysis. The basic premise of the box inverse is to adjust the strength of the reference velocity at each station pair so that constraints are satisfied within a given uncertainty (Section 3.2). In addition in this study, the box inverse allows for a correction to initial estimates of the mixing between neutral density layers, air sea fluxes and an Ekman transport. All diapycnal fluxes associated with interior mixing or air-sea induced transformation are initialised to zero (McDonagh and King, 2005). As the solution that is estimated is dependent upon the initial field, it is important that the initial field is as representative as possible.

At Drake Passage, the reference level choice (Table 2) of the deepest common level between the station pairs is based on the analysis of the mean volume transport of multiple repeat stations across Drake Passage of $136.7 \pm 6.9 \text{ Sv}$ (Cunningham et al 2003, Meredith et al., 2011), Lowered Acoustic Doppler Current Profiler transport estimates (Meredith et al., 2011) and the scale of interannual variability (King and Jullion, in prep.). At 24°S, the 1300 dbar reference level approximates the upper water/NADW interface. At 30°E, Bryden et al. (2005) and Arhan et al. (2003) are used as a guide for the vertical transition between the Agulhas Current and Agulhas Return Current, and the Agulhas Undercurrent at depth (Beal and Bryden, 1999). On all sections the geostrophic

velocity within the ‘bottom triangle’ is set by nearest neighbour extrapolation to the deepest common level for each station pair.

For the 24°S section, Ekman transport from NCEP (National Centers for Environmental Prediction) wind stresses, an annual average calculated between 1980-2010 in Bryden et al. (2011), of 3.3 Sv southward is applied as a single velocity above the 80 dbar Ekman depth (D_{EK}). The Ekman component is included at 24°S as part of the initial field.

3.3 Constraints

3.3.1 Constraints to circulation and property transports on sections

The constraints across hydrographic sections, based on historical analyses and listed in Table 3, are applied to better constrain the initial field, and later used to constrain the box inverse model. Further details regarding the constraints in Table 3 are described below.

Across Drake Passage, full-depth volume transport is constrained to 136.7 Sv (Cunningham et al., 2003; Meredith et al., 2011).

Bottom Water (BW) across 24°S has been defined to be below the 2 °C isotherm (Hogg et al., 1999; McDonagh et al., 2002), shallower than the typical AABW neutral density class definition (neutral density: $\gamma^n > 28.27$) in the Southern Ocean, and partly includes the lower layers of the LCDW neutral density class within the Vema Channel and Hunter Channel. Northward BW flow is constrained following Hogg et al. (1999), Zenk et al. (1999) and McDonagh et al. (2002), as 6.9 Sv below the 2 °C isotherm. Within the northern Cape Basin, east of Walvis Ridge (6°E), a zero mass transport constraint is applied below the 2 °C isotherm (Arhan et al., 2003; McDonagh and King, 2005). For the sectionwide upper 80 dbar, a southward, wind-driven estimate for the Ekman transport of 3.3 Sv is included following Bryden et al. (2011). For the upper 300 dbar, west of 35°W, the Brazil Current is constrained to 4.9 Sv southward (Bryden et al., 2011). Finally, full depth salinity transport across 24°S is constrained to be equal to the Bering Strait salinity transport of 26.0 Sv psu, assuming salinity conservation (Coachman and Aagaard, 1988).

For the 30°E section, north of the Subtropical Front (42.9°S), the residual westward flow of warm, salty Indian Ocean water into the Atlantic Ocean or ‘Agulhas leakage’ is estimated based on McDonagh et al. (1999) as 9 Sv above the 3.5 °C isotherm. Finally, a box-wide constraint for zero net salinity divergence is applied by summing together salinity transport through the Agulhas regime, Drake Passage and across 24°S. Total salinity transport outflow across the 30°E ACC regime is adjusted to match the inflow across Agulhas regime, Drake Passage and 24°S (Table 3). The residual mass transport is interpreted as the freshwater flux of the initial field.

3.3.2 Property constraints in the box

Each transect is split into 21 neutral density (γ^n) layers (Table 4; Jackett and McDougall (1997)). Neutral density class interfaces, appropriate for the Southern Ocean, are extracted from Heywood and King (2002), Naveira Garabato et al. (2009, 2002a, 2002b) and Orsi et al. (1999, 1995). The layers are grouped into six neutral density classes. Each γ^n layer represents an equation to be solved for, with an additional row for the full depth water column. Conservation of mass, heat and salt (approximated as volume, potential temperature anomalies and salinity anomalies) for each layer plus full depth conservation gives 66 equations or constraints for the analysis. Additionally, full-depth silicate conservation plus 6 constraints from previous knowledge of the circulation (Table 3) gives a total of 73 constraints. Salinity and θ within each γ^n layer are conserved in the form of a property anomaly, calculated by subtracting each property value by the boundary-wide average, calculated using the whole domain boundary. The use of property anomalies improves the matrix conditioning (Ganachaud, 2003; McIntosh and Rintoul, 1997). For silicate, as argued by Ganachaud (1999), property anomalies are not calculated given the large concentration range between surface and deep waters. Loss of silicate through opal deposition is assumed negligible, given large uncertainties in the silicate budget (Tréguer and De La Rocha, 2013) with this assumption encouraging conservation within the silicate-rich bottom waters.

3.4 Solution

3.4.1 Unknown velocities

In this study, the columns of \mathbf{E} are constructed to solve for unknowns; geostrophic, diapycnal, air-sea fluxes and Ekman transports, and each row in \mathbf{E} represents an equation or constraint. In order to better condition the pre-inversion matrix for solving for the unknown velocities, each row and each column of the $m \times n$ coefficient matrix \mathbf{E} is weighted based on estimates of the previously known, ‘a priori’ uncertainties within each component (see Appendix A). Solution weightings are applied as stated in Appendix A following the method of McDonagh and King (2005) and Tsubouchi et al. (2012).

The geostrophic component of each cross-sectional station pair is applied with an a priori uncertainty of $1 \times 10^{-2} \text{ m s}^{-1}$, as in Naveira Garabato et al. (2003), McDonagh and King (2005) and Jullion et al. (2010). The a priori uncertainty is uniform for all station pairs across all transects.

For the inverse model, the Ekman transport adjustment is initialised as a single unknown. The coefficient matrix \mathbf{E} , initialised for a single unknown representative of the Ekman transport adjustment, is initialised by the area above D_{Ek} , the property mean of the Ekman layer, and the proportional contribution of the Ekman transport to each γ^n layer above D_{Ek} . As the climatological data contains uncertainties, which are difficult to quantify, an a priori uncertainty of 50% of the initial estimate of the Ekman transport adjustment is assigned.

3.4.1.1 Interior diapycnal velocities

A separate diapycnal velocity is resolved for each property (McIntosh and Rintoul, 1997) and for each layer interface. The interface mean for each property (S, θ) is generated using the WOCE Global Hydrographic Climatology (WGHC) by Gouretski and Koltermann (2004). The WGHC data is on a 0.5° grid, and averaged along isopycnal surfaces, such that the properties are broadly in agreement with the properties along the sections. The layer interface area for each of the neutral density interfaces in this study is constructed from the initial 45 levels from WGHC for each mapped property field. For the diapycnal mixing, a priori uncertainties are dependent on the pre-existing estimates of diapycnal velocities (ω) and assigned as 10^{-5} m s^{-1} , following Orsi et al. (1999) and

Naveira Garabato et al. (2003), for an estimate of an upper value for deep ocean diapycnal velocities.

3.4.1.2 Diapycnal transfers induced through Air-Sea interactions

Heating and cooling of neutral density classes, as the isopycnals outcrop at the ocean surface provides a mechanism for across isopycnal transformation (Speer and Tziperman, 1992; Tziperman and Speer, 1994). Within the Southern Ocean, all layers are assumed to outcrop given the upwelling of deep neutral density classes. Following Jullion et al. (2010a), net air-sea fluxes of mass (freshwater) M_v and heat M_θ are calculated for each layer, whilst the diapycnal volume flux induced by air-sea interaction F_v is included for each layer interface. The area of outcrop for each neutral density layer is estimated from monthly averaged sea surface temperature and salinity fields from World Ocean Atlas (WOA) on a 1° grid (Antonov et al., 2010; Boyer et al., 2005; Locarini et al., 2010). To ensure an area of outcrop for the densest γ^n layers, the area of outcrop for all LCDW and AABW layers was averaged, and this value was assigned to all LCDW and AABW layers.

Heat flux terms are supplied by monthly-averaged estimates from the National Oceanography Centre (NOC v2.0) climatology (Berry and Kent, 2011, 2009). Net heat flux Q_{net} is the sum of contributions from latent (Q_H) and sensible heat flux (Q_E), longwave flux (Q_{LW}) and shortwave flux (Q_{SW}) (Grist and Josey, 2003). The mean heat flux for the January-February-March (JFM) period is 65 W m^{-2} .

Freshwater flux is based on the climatologies recommended by Schanze et al. (2010): Global Precipitation Climatology Project (GPCP) for precipitation (Adler et al., 2003), and Objectively Analysed Ocean-Atmosphere Flux (OAFlux) for evaporation (Yu et al., 2008; Yu and Weller, 2007). Evaporation is subtracted by precipitation (E-P) at each grid point using the 2008 and 2009 estimates, before finding the inverse box model mean. A priori uncertainties are estimated to be 50% of the initial estimates. Uncertainties arise from the uncertainty of the climatologies as described in Lumpkin and Speer (2007), as well as from not considering the contribution of sea-ice near the Antarctic continent.

3.4.2 Choice of preferred solution

The solution rank of 60 out of 73 is chosen after application of SVD. Truncation to the solution rank occurs at the point at which the noise added by including additional rows negates the information gained. The co-dependency between ocean layers gives reason for selection of a solution rank below the full rank. Ranks $\sim >50$ are suitable solutions with a full depth volume transport $\sim <1$ Sv, equivalent to the freshwater divergence. Reference velocities for the geostrophic component are generally within ± 0.5 cm/s with all adjustments off continental shelves within ± 0.7 cm/s.

3.5 Model Diagnostics

3.5.1 Overturning freshwater and heat transport

The overturning component of the salinity transport at 24°S is calculated for comparison to the outputs of Bryden et al. (2011) using the M_{ov} salt transport, in addition to the azonal component M_{az} . Additionally the heat transport associated with the ‘overturning’ and ‘gyre’ components is separated following the methods of Bryden and Imawaki (2001) and Bryden et al. (2011).

For freshwater, values for M_{ov} and M_{az} are calculated following Bryden and Imawaki (2001), Dijkstra (2007), Huisman et al. (2010) and Bryden et al. (2011):

$$M_{ov} = - \frac{1}{\langle S \rangle} \int \langle v \rangle (\langle S \rangle - \overline{\langle S \rangle}) L(z) dz \quad (9)$$

$$M_{az} = - \frac{1}{\langle S \rangle} \iint (v - \langle v \rangle) (S - \langle S \rangle) dx dz \quad (10)$$

where v is the northward velocity, S is salinity, L is zonal section width and z is depth. Triangular brackets indicate a zonal average and an overline represents a vertical average. The M_{ov} and M_{az} transports are effectively the freshwater transports associated with the overturning and gyre circulation components, respectively. Cimadoribus et al. (2012) suggest that an increase in the zonal salinity contrast across the South Atlantic increases M_{az} and that this is compensated by a decrease in M_{ov} . Changes in M_{az} could therefore dictate potential MOC shutdown (Cimadoribus et al., 2012).

The volume transports and overturning freshwater transports associated with the MOC are detailed in section 4.1. Geostrophic and non-geostrophic results are described and circulation features examined in section 4.2. For section 4.3, C^{ant} transports are calculated for each layer, whilst C^{ant} air-sea flux is considered in section 4.3.3.

4 Inverse Model Solution

4.1 Volume and overturning freshwater transports

4.1.1 Geostrophic solution

The geostrophic velocities of the final solution are shown in Figure 2. The overall velocity pattern is for strong flow into the box through Drake Passage and an outflowing velocity along 30°E , south of the Subtropical Front. North of the Subtropical Front, positive and negative velocities reflect the Agulhas Current inflow and Agulhas Return Current outflow. The box-wide salinity transport conservation results in a net volume imbalance of -0.47 Sv, interpreted as a loss of freshwater, balanced by excess precipitation over the box.

The net transport (Figure 3, right) indicates convergence (positive numbers) or divergence (negative numbers) of a neutral density class within the box. Convergence can be interpreted as destruction of that neutral density class within the box and divergence reflects production of that neutral density class. Basinwide UCDW layer convergence is caused by upwelling of the MOC southern limb (see Section 4.1.2.1), resulting in northward flowing surface and mode water and AABW layer formation to the south. LCDW layer divergence corresponds with greater outflow across 30°E (44.4 Sv) compared to Drake Passage inflow (28.1 Sv), caused by mixing the NADW and AABW layers with the LCDW layer.

4.1.1.1 Drake Passage

The final solution decreases the Drake Passage initial field full-depth volume transport of 136.7 ± 10 Sv to 128.4 ± 8.3 Sv (Table 3). This is within the uncertainty of the volume transport, estimated as 126.3 - 147.1 Sv (King and Jullion, in prep., and Meredith et al. (2011) (their Figure 11)). Transport of UCDW layers constitutes almost half of the Drake

Passage full depth volume transport (58.1 Sv out of 128.4 Sv; Figure 3), in agreement with the 62.3 Sv estimate of Cunningham et al. (2003), relative to the deepest common level. Within the SACCF, the transport is equally split between UCDW and LCDW layers. The contribution of SAMW and AAIW layer transport increases progressively to the north along the section.

4.1.1.2 24°S

For the Brazil Current, the final solution of 5.8 ± 0.1 Sv falls within the historical range as described in Bryden et al. (2011) with the salty Brazil Current being important for the total salinity transport across 24°S. Bottom water exchange from the northern Cape Basin into the eastern South Atlantic basin is limited by Walvis Ridge. The final solution shows 0.2 ± 0.1 Sv of southward AABW layer transport, and is similar to McDonagh and King (2005)'s estimate of 0.1 ± 0.5 Sv.

The southward basin-wide full-depth salinity transport at 24°S (25.8 ± 0.2 Sv psu, Table 3) closely matches observations from the Bering Strait throughflow (Coachman and Aagaard, 1988; Woodgate and Aagaard, 2005) and is similar to Holfort and Siedler (2001)'s 26.75 ± 0.77 Sv southward salinity transport for the quasi-zonal A10 WOCE section across 30°S. Historical meridional freshwater, heat and salt transports across 24°S, 30°S and 32°S are included for comparison with the results from our box inverse (Table 5). Focussing firstly on net freshwater transport, the difference between 0.8 Sv Bering Strait volume transport and the southward 0.7 Sv volume transport at 24°S provides an indirect 0.1 Sv estimate for freshwater divergence between Bering Strait and 24°S. Figure 4, adapted from Piecuch and Ponte (2012), compares hydrographic estimates of meridional heat transport, following Hall and Bryden (1982), within the Atlantic Ocean. The estimate from this study is added (marked with a red point), calculated by adjusting the inverse model solution to yield zero net mass transport along 24°S by adding an additional barotropic velocity. The estimate of 0.40 ± 0.08 PW out of the box is within the range of the anticipated heat transport across 24°S.

In order to assess the overturning circulation, each of the 21 γ^n layers (Table 4) is grouped, depending on flow direction. The circulation consists of 0.8 ± 4 Sv of southward flowing surface water (layers 1-2), as a result of the Ekman transport, 15.8 ± 3 Sv northward flow of upper ocean water (layer 3-12), 20.2 ± 2 Sv southward flow of deep water (layers 13-18) and 4.6 ± 1 Sv northward flow of lower LCDW and AABW (layers 19-21). The MOC strength is estimated as the 20.2 Sv southward flow of deep water, comparable with the previous estimates in Table 5.

4.1.1.3 30°E

On the 30°E section north of 34°S, strong westward flow of warm, salty Indian Ocean water close to the continental slope results in a total westward transport of 65.7 Sv (Figure 3), similar to findings by Casal et al. (2009). Between ~ 34 -35°S, westward transport is interrupted by eastward flow. The maximum westward flow is 84.5 ± 2.0 Sv for the Agulhas Current. The Agulhas Return Current is attributed to the net eastward flow south of $\sim 36.25^\circ$ S, occupying a broader meridional extent compared to the Agulhas Current. The Agulhas Return Current transport is estimated as 82.2 ± 2.0 Sv, extending between 36.25°S and the Subtropical Front (42.9°S). Above 3.5 °C, a 10.7 ± 1.3 Sv Agulhas leakage is detected, comparable with an estimate of 15 Sv from observations using subsurface floats and surface drifters (Richardson, 2007).

South of the Subtropical Front (STF), the net eastward transport of 131.7 Sv is dominated by the ACC. This estimate is lower than the previous estimates of 160 Sv (full 30°E section, Park et al. (2001)), 147 ± 10 Sv (STF to SACCF between 0°E and 30°E, Legeais et al. (2005)), 136 Sv to 153 Sv for baroclinic and total transport (north of 54.75°S between 0°E and 20°E, (Gladyshev et al., 2008)) and 141.6 ± 2.9 Sv along 30°E (Naveira Garabato et al., 2014). The estimate is closer to the Drake Passage volume transport, as a consequence of constraining the salinity transport around the box boundary. Significant westward flow of AABW is predominately associated with the westward-flowing southern limb of the Weddell Gyre, as previously observed by Schröder and Fahrback (1999), Park et al. (2001) and Jullion et al., (2014) along the Antarctic continent at 0°E and 30°E.

4.1.2 Non-geostrophic terms

4.1.2.1 Diapycnal transfer of volume, freshwater and heat in the ocean

interior

A positive diapycnal volume flux represents an upward diapycnal transfer from a denser neutral density class to a lighter neutral density class. In this study, the net diapycnal velocities and volume fluxes (Figure 6a-b) indicate that diapycnal transfer is primarily within the denser layers with nearly zero diapycnal volume flux for layer 10 and above. The vertical structure becomes more significant within the UCDW layer with a tendency for positive fluxes of up to 1 Sv suggesting diapycnal upwelling, including for NADW defined as at the UCDW/LCDW interface ($27.90 < \gamma^n < 28.10$), equal to layers 16 and 17 (Table 4). The lighter LCDW layer also upwells (4.9 Sv), whilst the most significant downwelling signal of 2 Sv contributes to the production of the densest LCDW layer. The production within this layer is furthered by significant upwelling of 6.3 Sv of AABW layer to LCDW layer with a diapycnal velocity of $\sim 1.5 \times 10^{-5} \text{ m s}^{-1}$. The rough topography of the Scotia Sea (Heywood et al., 2002; Naveira Garabato et al., 2004), and deep passages, such as Vema Channel (Morris et al., 2001), potentially contribute to the significant upwelling and mixing of the AABW and LCDW layers. The absence of large scale diapycnal flux of NADW to lighter neutral density classes supports the findings of Sloyan and Rintoul (2001) for deep to intermediate water conversion in the Southern Ocean to occur along isopycnals, rather than by uniform interior upwelling as suggested in historical conceptual models (e.g Munk, 1966; Gordon, 1986).

Upward diapycnal salinity flux (Figure 6d) from the SAMW layer towards the fresher surface water and downward diapycnal salinity flux towards the AAIW layer implies a divergence of salinity from the SAMW layer. The SAMW layer is relatively salty in comparison to the waters above and below. This salty SAMW signature is consistent with SAMW sourced from the inflow of salty Indian Ocean water south of Africa, as opposed to fresher SAMW through Drake Passage, in agreement with Sloyan and Rintoul (2000). A similar, if smaller divergence of the salinity flux is observed for the NADW layer at the UCDW/LCDW boundary. Upwelling of salinity to lighter UCDW layers, and

downwelling to denser LCDW layers, contributes to the erosion of the NADW salinity maximum.

Diapycnal temperature velocities (Figure 6f) greater than 0.1 m s^{-1} are only found within the LCDW and AABW layers. For the temperature fluxes, the contribution from diffusion results in the upwelling of temperature flux from denser to lighter LCDW layers, and the downward mixing of LCDW temperature flux to the AABW layer.

4.1.2.2 Diapycnal transfer of volume, freshwater and heat by Air-Sea interaction

Air-sea interaction contributes to the formation of 14.6 Sv of SAMW through the AAIW to SAMW flux in Figure 7a. This matches (despite the difference in area) the 14 Sv estimate of Sloyan and Rintoul (2001) for their South Atlantic box, nominally bounded by transects at Drake Passage, 0°E and $12\text{-}19^\circ\text{S}$. This process is hypothesised to dominate within the southwest Atlantic region, in the vicinity of the energetic Brazil-Malvinas Confluence (BMC) (Jullion et al., 2010a). Convergence of dense surface water/SAMW is approximately compensated by the divergence of deep neutral density classes: UCDW and upper LCDW ($\sim 15.2 \text{ Sv}$; c.f. 8 Sv (Sloyan and Rintoul, 2001b)). Upwelling of lighter deep neutral density classes, primarily UCDW, and transformation to SAMW/AAIW via exposure to wind, heat and freshwater fluxes contributes towards the MOC southern limb.

Net freshwater flux contributes to volume flux induced by air-sea interaction, and reflects adjustments to the initial freshwater flux estimate, with extra evaporation required from the surface water layer. As described in Jullion et al. (2010a), freshwater flux is difficult to estimate accurately given uncertainties in upper ocean baroclinic variability and therefore the a priori uncertainties applied to the inverse box model (Ganachaud, 2003; Naveira Garabato et al., 2003).

Air-sea heat fluxes are dominated by the higher temperature surface ocean within the western South Atlantic basin (Figure 7c). Air-sea heat flux adjustments reach -0.53 PW

for radiative heat loss from the warm uppermost surface layer, as it moves northwards towards the North Atlantic Ocean. However, over the water column, the total net adjustment is -0.07 PW for the net air-sea heat flux input estimate of 2.15 PW (65 W m^{-2} over the South Atlantic area) as denser surface layers are heated by the atmosphere. Therefore whilst the whole column adjustment is insignificant, alterations for individual layers show greater significance. Small overall adjustments suggest good agreement between the NOC (v2.0) climatology and observations, despite variability between NOC (v2.0) climatology and alternative heat flux climatology products, particularly in the Southern Ocean (Liu et al., 2011).

4.1.2.3 Ekman

The model diagnoses Ekman transport adjustments, assumed meridionally uniform across 24°S , in addition to the initial field Ekman transport. Total volume transport adjustment is 0.5 Sv contributing towards the 0.7 ± 0.3 Sv freshwater flux. Given uncertainty within the NCEP wind stress (Brunke et al., 2011) used to derive the initial field Ekman transport, the additional transport associated with the Ekman adjustments is only significant within the context of ensuring a net salinity transport of about 26 Sv psu across 24°S .

4.2 South Atlantic circulation

Schematic circulation of geostrophic flow within the South Atlantic is shown in Figure 8 for the upper and deep ocean neutral density classes. Conversion of the AAIW layer to surface water and SAMW layers occurs between Drake Passage and the 30°E ACC regime. Accumulation within the LCDW layer between Drake Passage and 30°E is offset by AABW layer inflow, as part of the Weddell Gyre southern limb. These results also suggest that the entrainment of the AABW layer into the Circumpolar Deep Water layer is more significant than the intermediate to deep water conversion based on the convergence of the AABW layer at the box boundary.

Within the subtropics, surface water and SAMW entering the South Atlantic through the Agulhas regime is entrained at the South Atlantic Current/Benguela Current transition,

and joins the northward pathway for Agulhas-sourced upper ocean water across 24°S. Given a southward flow of 18.1 Sv of deep water (UCDW and LCDW) across 24°S, the eastward flow of 5.9 Sv of deep water across the Agulhas regime proportionally accounts for approximately one-third of the deep water exiting the South Atlantic that entered the South Atlantic across 24°S. The remainder of the deep water flows into the Southern Ocean and contributes to both Circumpolar Deep Water, and the MOC southern limb.

4.2.1 North Atlantic Deep Water layer circulation

For the NADW layer (Figure 9), defined as $27.90 < \sigma^{\theta} < 28.10$, the box-wide circulation is as follows. A net excess inflow from the sum of the box boundary transports requires the divergence of 7.5 Sv from the NADW layer, predominately by upwelling to lighter neutral density classes. This broadly matches the estimate of diapycnal fluxes induced by air-sea interaction of 7.3 Sv from Figure 7a for the NADW layer (layers 16, 17).

4.2.2 Antarctic Bottom Water sources and recirculation

A significant source of AABW formation at the Cape Darnley polynya (65°E - 69°E) (Meijers et al., 2010, Ohshima et al., 2013) contributes to full depth cumulative transport of 15.9 ± 2.3 Sv (Figure 3) for the westward flowing, Weddell Gyre southern limb, south of 64.25°S (Naveira Garabato et al., 2014, 2002a). This is largely comprised of LCDW (6.3 ± 1 Sv) and AABW (8.8 ± 0.5 Sv), and comparable to the 24 ± 4 Sv flow associated with the Antarctic Slope Front by Jullion et al. (2014) or 9.6 ± 2.3 Sv Antarctic Slope Front estimate by Dong et al. (2016). Within the Weddell Sea, LCDW and AABW are modified and subsequently exported northward, with wind-forcing thought to dominate this process (Gordon et al., 2010; Jullion et al., 2010b; Wang et al., 2012). Comparatively, the recirculating northern limb of the Weddell Gyre shows a much weaker eastward AABW layer flow across 30°E (Figure 3). The difference between the 8.8 ± 0.5 Sv inflow of the AABW layer, as part of the Weddell Gyre southern limb, and the smaller AABW layer outflow across 24°S of 2.6 ± 0.5 Sv is, at least, partially offset by 6.3 ± 1.0 Sv of diapycnal upwelling to the densest LCDW layers. This contributes to a 6.7 ± 2.2 Sv northward flow, below the 2 °C isotherm, west of the Mid-Atlantic Ridge

(10°W), whilst the remaining AABW layer is hypothesised to recirculate within the South Atlantic box.

4.2.3 Overturning and gyre circulation for heat and freshwater

The overturning component (Table 6a) is particularly sensitive to the Ekman transport (assumed uniform across the section initially) and initial constraints on the Brazil Current transport. Both components of the total heat transport were similar to those estimated by Bryden et al. (2011).

The M_{ov} estimates (Table 6b, Figure 5a) are similar to Bryden et al. (2011) and indicate a net southward freshwater transport. Positive M_{az} in this study and Bryden et al. (2011), corresponds with the gyre and the flow near the boundaries transporting freshwater out of the South Atlantic box (Figure 5b).

4.3 Anthropogenic Carbon

4.3.1 Distributions

The Drake Passage C^{ant} distributions in Figure 10 are calculated using the ΔC^* method, with the C^{ant} transports in section 4.3.2 all calculated using the 2009 transect. This transect indicates C^{ant} concentrations markedly shallow from north to south, partly following the general trend of the neutral density isopycnals. The transect maximum of $>30 \mu\text{mol kg}^{-1}$ is primarily within surface, SAMW and AAIW neutral density classes with negligible C^{ant} for the AABW neutral density class. Across 30°E (Figure 11), higher concentrations ($>25 \mu\text{mol kg}^{-1}$) are either found within the Agulhas regime down to 1000 dbar or within the upper 200 dbar, south of the Agulhas regime. C^{ant} transports in this study, all make use of the 2008 transect across 30°E. Across 24°S (Figure 12), lower concentrations ($<10 \mu\text{mol kg}^{-1}$) are predominately below 1000 dbar.

4.3.2 Transports

Total C^{ant} fluxes of individual neutral density classes are controlled by the underlying volume transport. Net imports of C^{ant} into the South Atlantic box occur only through Drake Passage (Table 7, Figure 13). Across 24°S, although total net DIC flow is

southward (Gruber et al., 2009), the large surface-to-deep C^{ant} gradient causes a net northward transport, in line with previous estimates (Holfort et al., 1998). A C^{ant} overturning estimate of 0.11 PgC yr^{-1} , associated with the 20.2 Sv overturning, is calculated based on the southward transport of C^{ant} -poor deep water (layers 13-18 following Section 4.1.1.2). A net eastward C^{ant} transport within the Agulhas regime is caused by ventilation within the highly energetic South Atlantic sector of the Agulhas regime and C^{ant} increase in the upper ocean, prior to the eastward return flow.

The mean transport-weighted (TW) C^{ant} is calculated for each neutral density class at the box boundaries by dividing the total C^{ant} transport by the total volume transport (Table 8). Transport-weighted values are most heavily weighted at the location of the transport maximum, and hence are directly influenced by changes in the transport profile (Georgi and Toole, 1982; Tillinger and Gordon, 2010). Neutral density classes with the largest volume transports along both Drake Passage and the 30°E ACC regime, particularly UCDW and LCDW layers (Figure 8), therefore contribute significantly to the observed C^{ant} divergence (Figure 13). Small systematic biases within these low C^{ant} waters, below the level of the adjustments calculated as part of GLODAPv2, could contribute towards the significant C^{ant} divergence. The C^{ant} divergence shown by larger eastward-flowing TW C^{ant} at 30°E, compared to either eastward-flowing TW C^{ant} at Drake Passage or southward-flowing C^{ant} at 24°S is suggestive of an air-sea C^{ant} input requirement.

Storage rate is calculated using MPD estimates from Drake Passage, 24°S and 30°E multiplied by the mean rate of C^{ant} increase in the mixed layer (Table 9). As listed in Table 9, MPD from Drake Passage and 30°E are notably shallower than 770m for the region between 10°S and 30°S (Holfort et al., 1998), and 790 m at 24.5°N (Rosón et al., 2003). As described in Álvarez et al. (2003), areas with higher stratification yield shallower MPD, with comparatively lower penetration of C^{ant} below the upper 2000 dbar at Drake Passage, compared to 30°E, resulting in the shallower MPD. Increased convection, therefore leads to increased uncertainty in the time variability of the MPD (Khatiwala et al., 2013; Pérez et al., 2008).

Storage rates of $0.22 \pm 0.29 \text{ mol m}^{-2} \text{ yr}^{-1}$ along Drake Passage, $0.81 \pm 0.53 \text{ mol m}^{-2} \text{ yr}^{-1}$ along 24°S and $0.29 \pm 0.18 \text{ mol m}^{-2} \text{ yr}^{-1}$ along 30°E extend the range of previous South Atlantic storage rate estimates from repeat hydrography (Table 10). The values show similarities with the time-averaged Green's Function Inversion in Khatiwala et al. (2013) (their Figure 7). The Drake Passage estimate reflects its shallower MPD of 259.8 m than for other parts of the Southern Ocean, given that less C^{ant} has penetrated into deeper neutral density classes based on the lower TW C^{ant} estimates for UCDW, LCDW and AABW (Table 8). Along 30°E , the C^{ant} values are normalised by temperature to remove biases caused by cooler temperatures within the mixed layer in the 2008 occupation compared to the 1996 occupation. The temperature normalisation reduced the initial high $\Delta C_{\text{ml}}^{\text{ant}}$ estimate of $1.52 \text{ } \mu\text{mol kg}^{-1} \text{ yr}^{-1}$ along 30°E to $0.45 \text{ } \mu\text{mol kg}^{-1} \text{ yr}^{-1}$. The $0.45 \text{ } \mu\text{mol kg}^{-1} \text{ yr}^{-1}$ estimate is at the lower range of previous South Atlantic estimates of CO_2 uptake ($0.6\text{-}1.0 \text{ } \mu\text{mol kg}^{-1} \text{ yr}^{-1}$) (Murata et al., 2008; Peng and Wanninkhof, 2010; van Heuven, 2013). The 24°S estimate is similar to Holfort et al. (1998)'s estimate of $0.59 \pm 0.12 \text{ } \mu\text{mol kg}^{-1} \text{ yr}^{-1}$ for the 10°S and 30°S region and within their 20% uncertainty estimate.

For the South Atlantic box, the mean storage rate for Drake Passage, 24°S and 30°E (Table 10), calculated from the mean MPD, mean $\Delta C_{\text{ml}}^{\text{ant}}$ and mean ρ_{ml} (Table 9) and integrated over the ocean surface area (estimated as $3.3 \times 10^{13} \text{ m}^2$ assuming a parallelepiped ocean) yields a basin-wide C^{ant} storage of $0.18 \pm 0.12 \text{ Pg C yr}^{-1}$. Application of the TSR-based C^{ant} storage estimation method, which makes use of additional historical hydrographic cruise data from the interior of the South Atlantic Ocean sector, generates a storage term of $0.21 \pm 0.06 \text{ Pg C yr}^{-1}$ (van Heuven, S. (2016), manuscript in preparation). The two estimates compare well despite substantially different methodologies. The smaller TSR uncertainty represents its greater robustness as a calculation approach, due to the additional data and lack of structural assumptions compared with the MPD method (transient steady state, parallelepiped ocean). Historical storage estimates for the South Atlantic regions show slightly higher values: $0.30 \text{ Pg C yr}^{-1}$ between 2°S - 58°S based on decadal hydrographic observations (Peng and Wanninkhof, 2010) and $0.29 \text{ Pg C yr}^{-1}$ between 0°S - 58°S from multiple global ocean inversions based on hydrographic section data (Mikaloff Fletcher et al., 2006). Based on

this study, usage of MPD calculations appear to have some value in providing a reasonable estimate for C^{ant} storage in the absence of full basin-scale historical data. However, greater uncertainty will be assigned to estimates if the sampling pattern of the hydrographic cruises chosen does not fully capture the north-south variability within the Southern Ocean of the column inventory of ΔC^{ant} (see Figure 7.13 from van Heuven, (2013)). Similarly, MPD calculations are also dependent upon the shape of the C^{ant} profile, such that the presence of increasing amounts of C^{ant} within bottom water layers (due to proximity to bottom water ventilation locations) may compromise the MPD assumption (Khatiwala et al., 2013; Pérez et al., 2008). However, the sections used here are not thought to suffer from this at this stage, with negligible bottom-water C^{ant} change identified (Evans, 2013).

4.3.3 Anthropogenic CO₂ air-sea flux

The C^{ant} budget for the South Atlantic box - comprising storage and divergent flux terms at the box boundaries (Figure 13) - is balanced by a $0.51 \pm 0.37 \text{ Pg C yr}^{-1}$ air-sea flux term. This compares to a global anthropogenic CO₂ uptake of 2.2 to $2.6 \pm 0.3 \text{ Pg C yr}^{-1}$ estimated from ocean inverse and biogeochemical models (DeVries, 2014; Gruber et al., 2009), or more generally 2 Pg C yr^{-1} from a range of oceanic and atmospheric observations (Wanninkhof et al., 2013). The Southern Ocean is the largest annual sink region of total (natural and anthropogenic) CO₂ of more than $0.42 \text{ Pg C yr}^{-1}$ south of 44°S (Lenton et al., 2013). Regional observations and model outputs for its Atlantic sector combined within the South Atlantic from 18-58°S, broadly similar to our South Atlantic box but excluding the small sea-air CO₂ flux south 58°S (Lenton et al., 2013; van Heuven, 2013), suggest a net annual mean total (natural and anthropogenic) CO₂ flux of $0.19 - 0.38 \text{ Pg C yr}^{-1}$ (Lenton et al., 2013; Schuster et al., 2013). This is smaller than the air-sea uptake estimate derived here that only quantifies the anthropogenic component. However, large outgassing of natural carbon identified in the Southern Ocean (Mikaloff Fletcher et al., 2007) suggests that any estimates of regional CO₂ uptake here will be disproportionately of anthropogenic origin. A global ocean circulation inverse model assimilating potential temperature, salinity, CFC-11 and radiocarbon observations (DeVries, 2014) supports the distinction between natural and anthropogenic CO₂ uptake,

with an estimated total (natural and anthropogenic) CO₂ uptake for the South Atlantic box of 0.43 Pg C yr⁻¹ of which 0.38 Pg C yr⁻¹ is anthropogenic CO₂. Although the air-sea C^{ant} uptake estimate here is larger than other observational and model estimates this is not entirely unexpected, as a seasonal bias may exist in the input C^{ant} estimates due to the austral summer-based cruise timings: increased stratification and intense biological production draw down surface carbon levels and increase the air-sea ΔpCO₂ difference. Combined with a temperature-related increase in the Revelle factor (Sabine et al., 2004) that enables greater anthropogenic carbon loadings, the associated uptake reaches its maximum during the summer months and is a likely major contributor to the large budget residual.

Differences from alternative estimates may also be partially methodological in nature. Given the large volume transports associated with the UCDW and LCDW neutral density classes in this study, systematic biases within these deep waters could potentially contribute to large differences in C^{ant} between Drake Passage and 30°E, which are inferred as being balanced by the air-sea flux. The differences between volume transport-weighted C^{ant} estimates at Drake Passage and 30°E (Table 8) also imply that these deeper neutral density classes must be gaining C^{ant} within the South Atlantic. Khatiwala et al., (2013) describe a key difference between the ‘ocean inversion’ method, where hydrographic section estimates of C^{ant} are combined with Ocean General Circulation Models (OGCMs), first applied in Gloor et al. (2003) and later in further depth in Mikaloff Fletcher et al. (2006, 2007), Gruber et al. (2009) and Khatiwala et al., (2013), and C^{ant} flux estimates from ship transects. Hydrographic occupations are accurate for a single point in time and thus subject to sampling biases, whilst the ocean inversion method represents a transport integrated in time since the industrial revolution, and typically scaled to any selected year (e.g. 1995 in Mikaloff Fletcher et al. (2006)). Additionally, seasonal variability affects hydrographic fluxes (Wilkin et al., 1995) with Lachkar et al. (2009) suggesting that subtropical South Atlantic seasonal variability corresponds to up to 20% of the annual mean transport of C^{ant}. The inverse model in the current study is designed to create a 2008-2009 ocean mean such that the calculated divergence within the South Atlantic Ocean is representative of that time period.

5 Conclusions

An inverse box model was used to examine net exchange between the South Atlantic Ocean and surrounding basins, inspired by the work of Rintoul (1991). We revisit this study with newer data and the inclusion of C^{ant} . The key findings include:

- The 15.9 Sv of westward Weddell Gyre return flow at 30°E contains 8.8 ± 0.5 Sv of the AABW layer, contributing to a net 13.8 ± 1.0 Sv inflow of the AABW layer to the box across all sections. Diapycnal upwelling of 6.3 ± 1.0 Sv from the AABW layer to the LCDW layer within the box, leads to a net AABW recirculation within the South Atlantic of 7.5 ± 1.4 Sv.
- A Meridional Overturning Circulation of 20.2 Sv with a net mass transport of 0.7 ± 0.3 Sv southward and a freshwater transport associated with the overturning component M_{ov} of 0.09 Sv southward across 24°S. This southward overturning freshwater flux of 0.09 Sv supports the notion of MOC bistability.
- Agulhas leakage, defined as westward flow above the 3.5 °C isotherm, is 10.7 ± 1.7 Sv. Total eastward transport of Circumpolar Deep Water is 5.9 ± 2.2 Sv beneath the Agulhas Current system, north of the Subtropical Front. Agulhas leakage contributes towards the northward flowing upper ocean water across 24°S, whilst up to one-third of southward-flowing deep water across 24°S, exits the South Atlantic underneath the net westward-flowing Agulhas leakage.
- The C^{ant} divergence from the South Atlantic box of 0.33 ± 0.31 Pg C yr⁻¹ and 0.18 ± 0.12 Pg C yr⁻¹ of C^{ant} storage correspond to a C^{ant} air-sea uptake of 0.51 ± 0.37 Pg C yr⁻¹. While 0.18 ± 0.12 Pg C yr⁻¹ of anthropogenic carbon is stored within the box, 89% of C^{ant} input to the South Atlantic box is exported from the South Atlantic. C^{ant} export from the South Atlantic occurs across both the 24°S section (0.28 ± 0.16 Pg C yr⁻¹), and across 30°E, associated with the 1.04 ± 0.42 Pg C yr⁻¹ ACC and the 0.08 ± 0.07 Pg C yr⁻¹ Agulhas Current and its return flow.
- Significant C^{ant} divergence within the South Atlantic box is only sustainable with significant C^{ant} uptake from the atmosphere. C^{ant} uptake of 0.51 ± 0.37 Pg C yr⁻¹ equivalent to approximately 25% of previous estimates of global C^{ant} uptake may be

caused through the upwelling of C^{ant} -poor NADW as part of the MOC, which subsequently absorbs atmospheric CO_2 into the ocean surface layers.

In conclusion, the South Atlantic circulation diagnosed in this study is characterised by inflow through Drake Passage, overturning south of 24°S consistent with southward-flowing UCDW and LCDW and conversion to lighter neutral density classes through diapycnal processes. Northward flows of surface water, SAMW and AAIW layers merge with a net westward Agulhas leakage from the Agulhas system to complete the MOC upper cell. AAIW, UCDW and LCDW flow eastward below the Agulhas system, whilst further south, eastward transport in the ACC dominates. Near the Antarctic continental margin, a westward flow supplies AABW to the Weddell Sea.

Ventilation and transformation within the Weddell Sea precedes the northward flow of the renewed AABW layer out of the Weddell Sea, whereupon significant diapycnal processes convert the AABW layer to the LCDW layer, limiting the volume of AABW exiting the South Atlantic. There is net SAMW production, LCDW layer creation and AABW layer destruction in the South Atlantic. For C^{ant} , an imbalance between the transport-weighted inflow and outflow for each neutral density class indicates significant uptake of CO_2 from the atmosphere within the South Atlantic, subsequently supplying the Atlantic Ocean north of 24°S and the Indian sector of the Southern Ocean with C^{ant} . Inter-basin exchange within the South Atlantic therefore ventilates CDW, receives, modifies and then consumes AABW, and supplies C^{ant} to the rest of the global ocean.

Appendix A

Constraint weighting

Each constraint has an associated uncertainty. As each constraint is represented by a row in **E**, each row is weighted according to the constraint's uncertainty. For the layer volume constraints, larger a priori uncertainties (ϵ_j) are applied to the upper ocean than the deep ocean following Ganachaud (2003) for the neutral density classes: Surface ($\pm 4\text{Sv}$), SAMW ($\pm 4\text{Sv}$), AAIW ($\pm 3\text{Sv}$), UCDW ($\pm 2\text{Sv}$), LCDW ($\pm 1\text{Sv}$) and AABW ($\pm 0.5\text{Sv}$). For volume transport constraints, the reciprocal of the a priori uncertainty is applied as the row weighting whilst for property transports, the reciprocal of the a priori uncertainty multiplied by 2, and multiplied by the larger of either the property standard deviation or property mean is applied for each layer/row. Typically a property standard deviation is applied, however, the property mean is included to cope with excessively small standard deviation values, and to better weight higher temperature anomalies within the surface waters across the box. For full depth salinity anomaly transport around the box boundary, a small a priori uncertainty (0.2 Sv psu) is applied to better constrain the system, making use of well-constrained values for Drake Passage (Cunningham et al., 2003; Meredith et al., 2011) and 24°S (Coachman and Aagaard, 1988; Woodgate and Aagaard, 2005), following the constraint for full depth boundary salinity transport applied to the initial field. The small uncertainty improves the zero salinity convergence constraint for the inverse box, rather than reflecting actual uncertainty. Only small full-depth residual imbalances for volume of -0.47 Sv and salinity anomaly of -1.08 Sv psu remain after applying the inverse box model.

Weightings for unknown velocities

The accuracy of the depth-independent velocities is affected by the inclusion of a priori uncertainties for weighting each column in **E**, and designed to optimally weight the different components of the solution. Column weighting takes the general form of the a priori uncertainty divided by the appropriate area and subsequently square rooted.

Appendix B

Historical surface data from five meridional cruises that intersect the 2009 24°S section across its full extent have been used to generate estimates of the change of anthropogenic carbon within the mixed layer (ΔC_{ml}^{ant}) and thus C^{ant} storage rates across 24°S, as detailed in Sections 2.1 and 4.3. Each meridional cruise provides a single intersection for comparison to the 24°S zonal transect. C^{ant} was calculated in an identical manner to the other box sections. The C^{ant} profile of the nearest station, in terms of latitude and longitudes coordinates, along each of the meridional sections is matched to the nearest station along the 24°S zonal transect to help determine ΔC_{ml}^{ant} . Historical cruises used were as follows: A14 (35A3CITHER3_1) occupying a longitude of 9°W at 24°S between January-February 1995 (Mercier and Arhan, 1995); A13 (35A3CITHER3_2) crossing through 24°S at 8°E between February-April 1995 (Mercier and Arhan, 1995); A15/AR15 (316N142_3) crossing 24°S at 19°W in May 1994 (Smethie and Weatherly, 1994); A16 (318HYDROS4) crossing 24°S at 25°W in March 1989 (Talley et al., 1989); and A17 (3230CITHER2_1-2) intersecting 24°S at 33°W in February 1994 (Mémery, 1994). Data from each of these cruises is accessible from the Carbon Hydrographic Data Office (CCHDO).

Acknowledgments

GRE thanks the Marine Physics and Ocean Climate group at the National Oceanography Centre, and the Natural Environment Research Council (NERC) for Ph.D. funding. ELM, BAK and the 24°S and Drake Passage Cruises were funded by NERC through Oceans2025 and SOFI (Strategic Ocean Funding Initiative). DCEB acknowledges funding for the Drake Passage cruise and subsequent analysis time from NERC Strategic Ocean Funding Initiative (SOFI) Carbon and Transient Tracers program (NE/F01242x/1) and European Union grant CarboChange (FP7 264879). PJB acknowledges funding from NERC Antarctic Deep Water Rates of Export (ANDREX) grant (NE/E013538/1). The 2008 I6S cruise was funded as part of the US repeat hydrography program, with principal funding from NSF grant OCE-0752970 and from NOAA. Additional support for KGS came from NSF OCE-1231803. GRE also thanks Takamasa Tsubouchi and Loïc Jullion for useful discussions on inverse methods, and Eric Achterberg, Andy Watson, Andrew

Yool and Chongyuan Mao for general comments. Help with data provision by Esa Peltola, Rik Wanninkhof and Mark Stinchcombe requires particular acknowledgment.

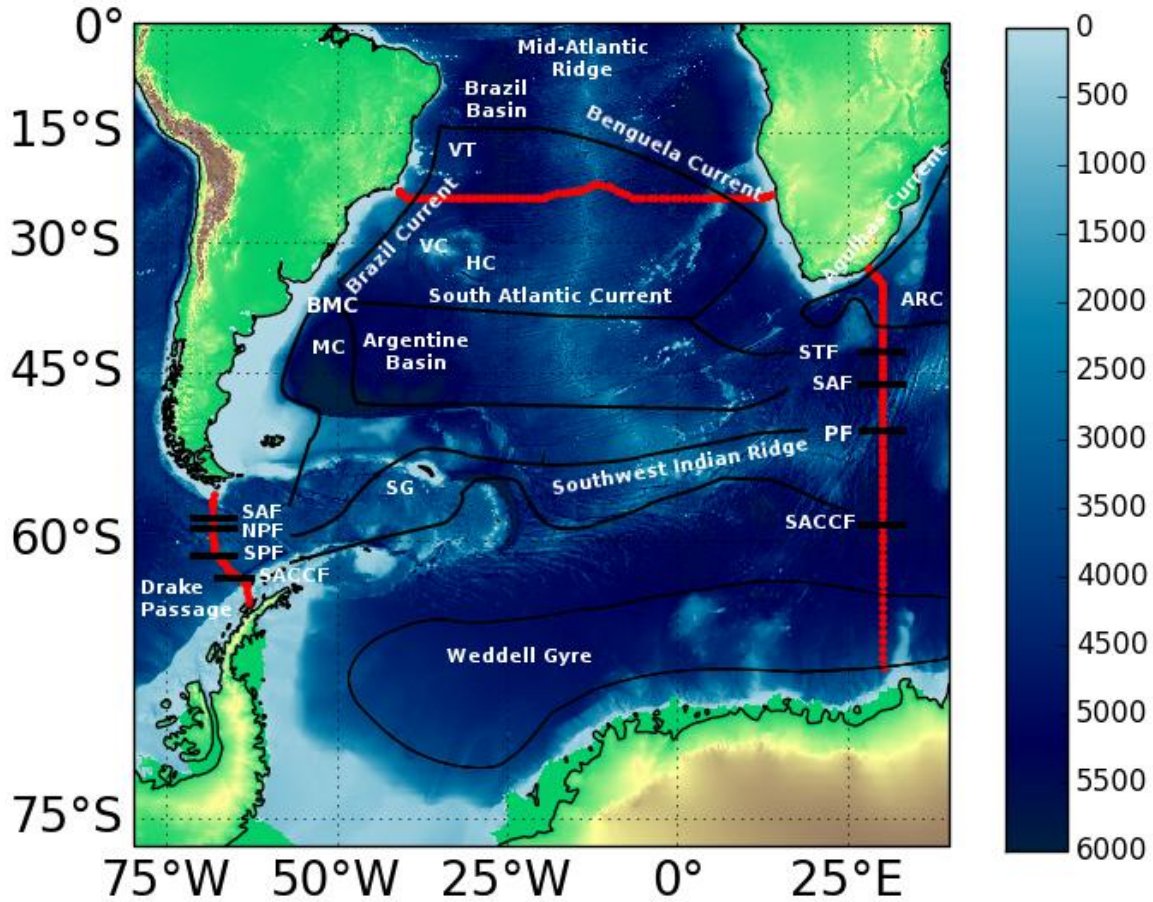


Figure 1: Map of the hydrographic sections that form the boundaries to the South Atlantic inverse box model. Sections are A21 (Drake Passage), I6S (30°E) and 24°S. The Subtropical Front (STF), Subantarctic Front (SAF), North Polar Front (NPF), South Polar Front (SPF) and Southern Antarctic Circumpolar Current Front (SACCF) are indicated. Major topographical and circulation features are: Vitoria-Trinidad seamounts VT, Vema Channel VC, Hunter Channel HC, Brazil Malvinas Confluence BMC, Malvinas Current MC, South Georgia SG and the Agulhas Return Current ARC.

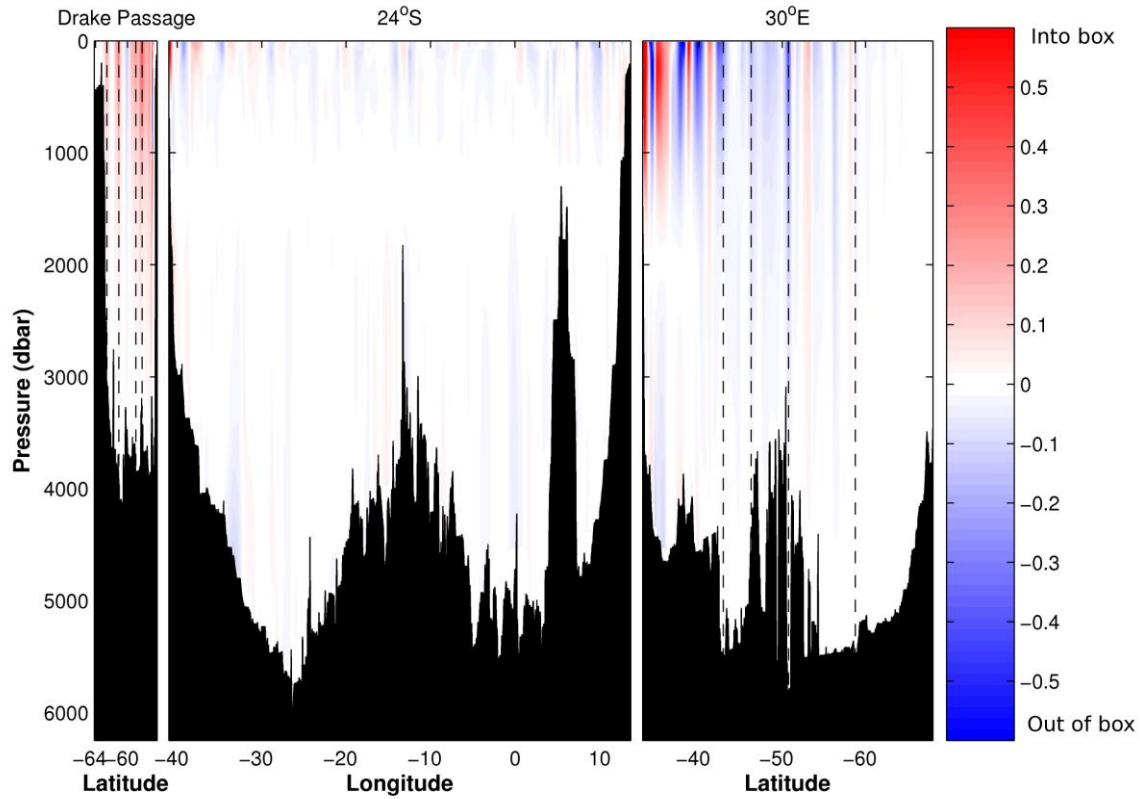


Figure 2: Geostrophic velocities (barotropic plus baroclinic velocities from the final solution) on the box boundary in units of m s^{-1} . Into (out of) the box is shown by red (blue). The dashed lines indicate frontal positions along the Drake Passage section from south to north: SACCF, SPF, NPF and SAF, and along the 30°E section from north to south: STF, SAF, PF, SACCF.

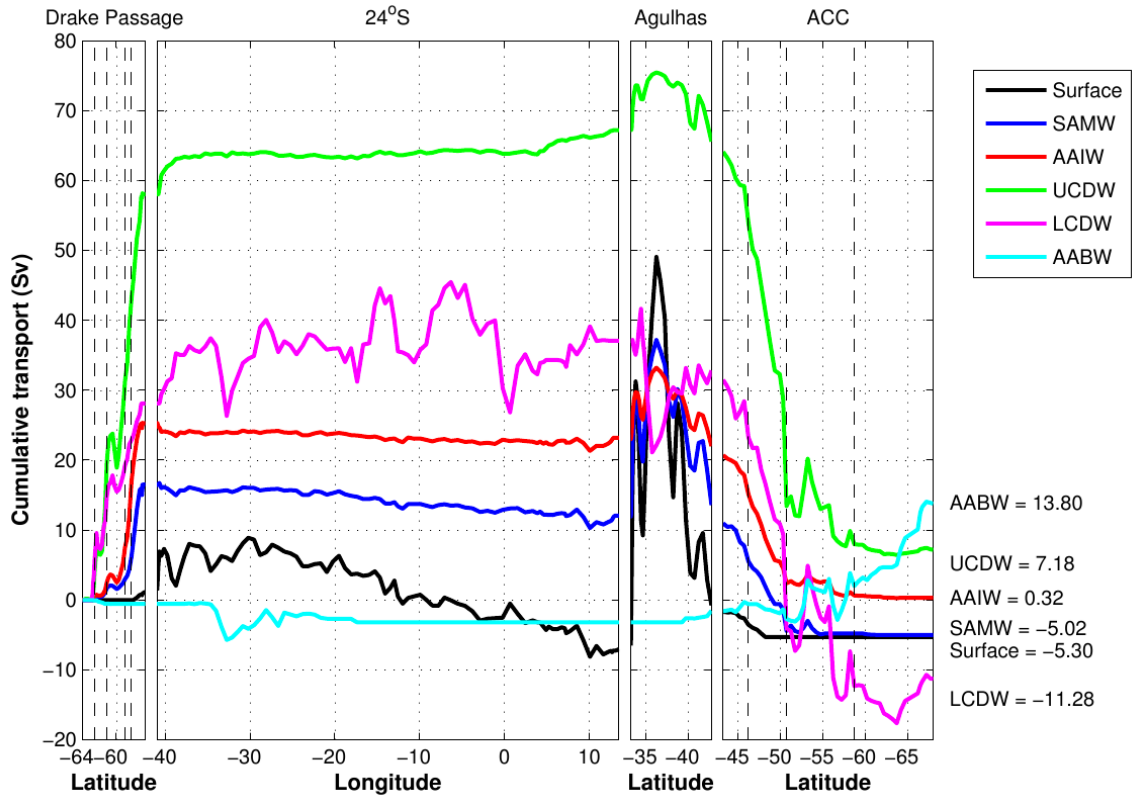


Figure 3: Cumulative transport along the box boundary for the final solution for each neutral density class in units of Sv. The total cumulative transport for each neutral density class is shown. Positive transports refer to a net gain by the box, whilst negative transports refer to a net loss. Vertical dashed lines indicate fronts.

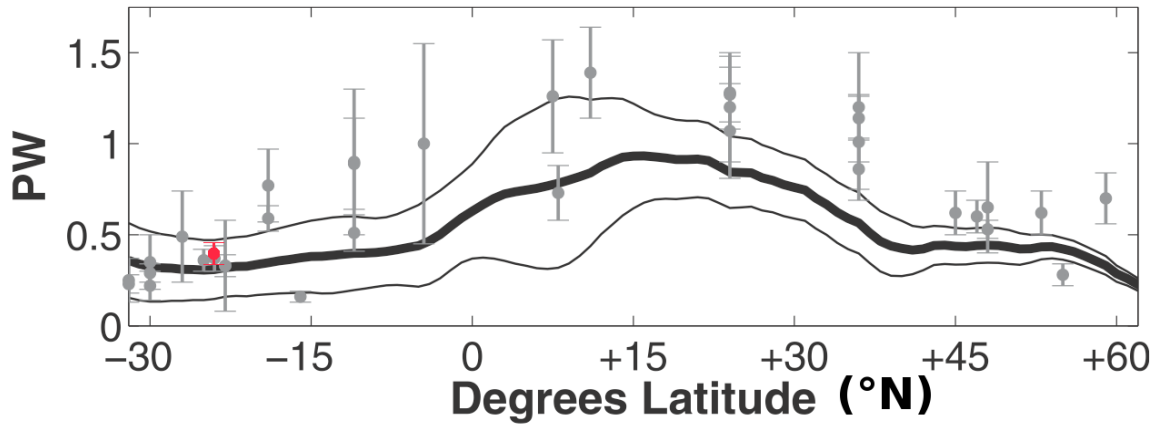


Figure 4: Heat transport (red; petawatts (PW)) for zero net mass transport across 24°S. Additional hydrographic estimates and errors (grey bars) are shown together with meridional heat transport (from Piecuch and Ponte (2012)) with an average time-mean ECCO (Estimating the Circulation and Climate of the Ocean; black solid thick line) estimate from model-observation syntheses. The uncertainty interval is given as the standard deviation of the heat transport time series (black thin lines).

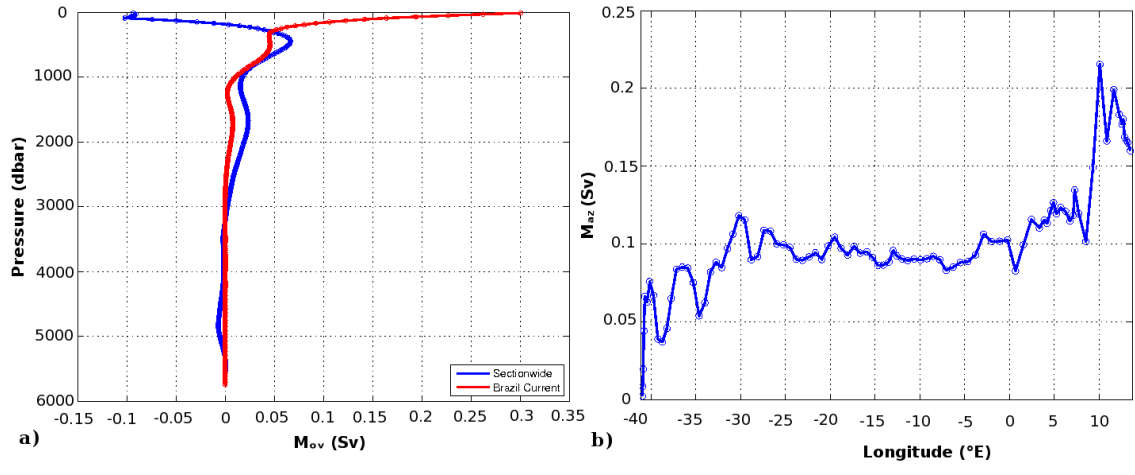


Figure 5: a) Cumulative M_{ov} as a function of pressure for the 24°S section (blue), and for west of 35°W, inclusive of the Brazil Current (red). Positive (negative) M_{ov} is northward (southward). Units of Sv. b) Cumulative M_{az} as a function of longitude. Positive (negative) M_{az} is northward (southward). Units of Sv.

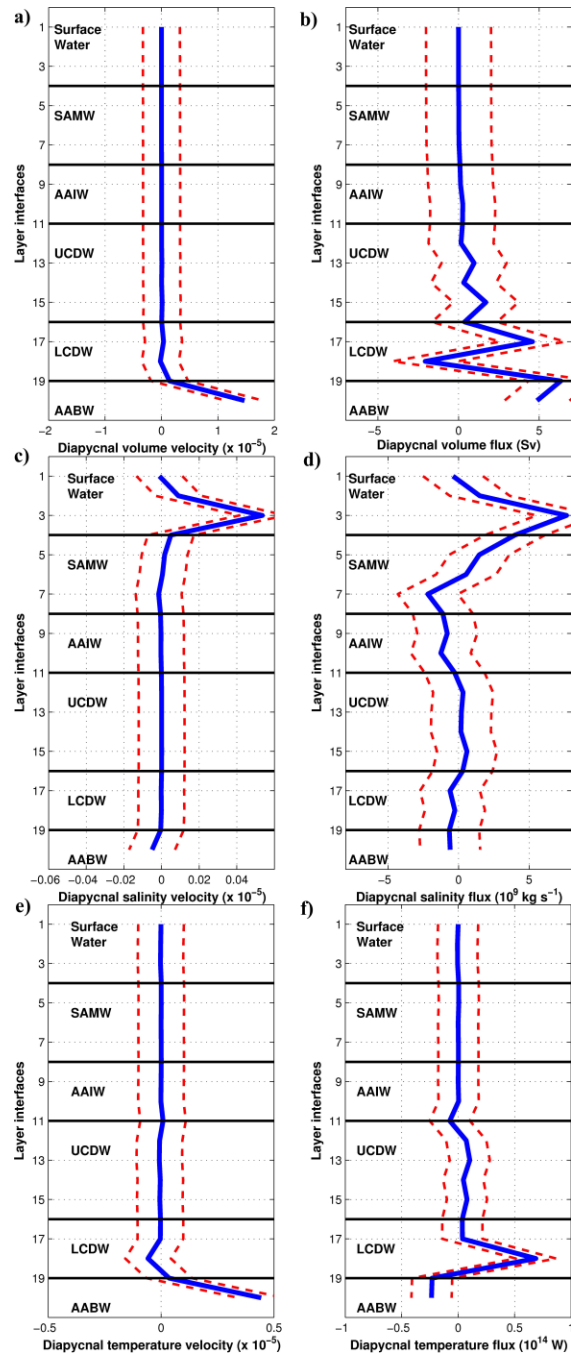


Figure 6: a) Diapycnal volume velocity (m s^{-1}) and b) volume flux (Sv), c) diapycnal salinity velocity (m s^{-1}) and d) salinity flux (kg s^{-1}) and e) diapycnal temperature velocity (m s^{-1}) and f) temperature flux (W) across each layer interface within the South Atlantic box. A positive (negative) velocity or transport represents an upward (downward) flow. The dashed lines represent one standard deviation. Neutral density class boundaries are marked (solid black line), and neutral density classes labelled.

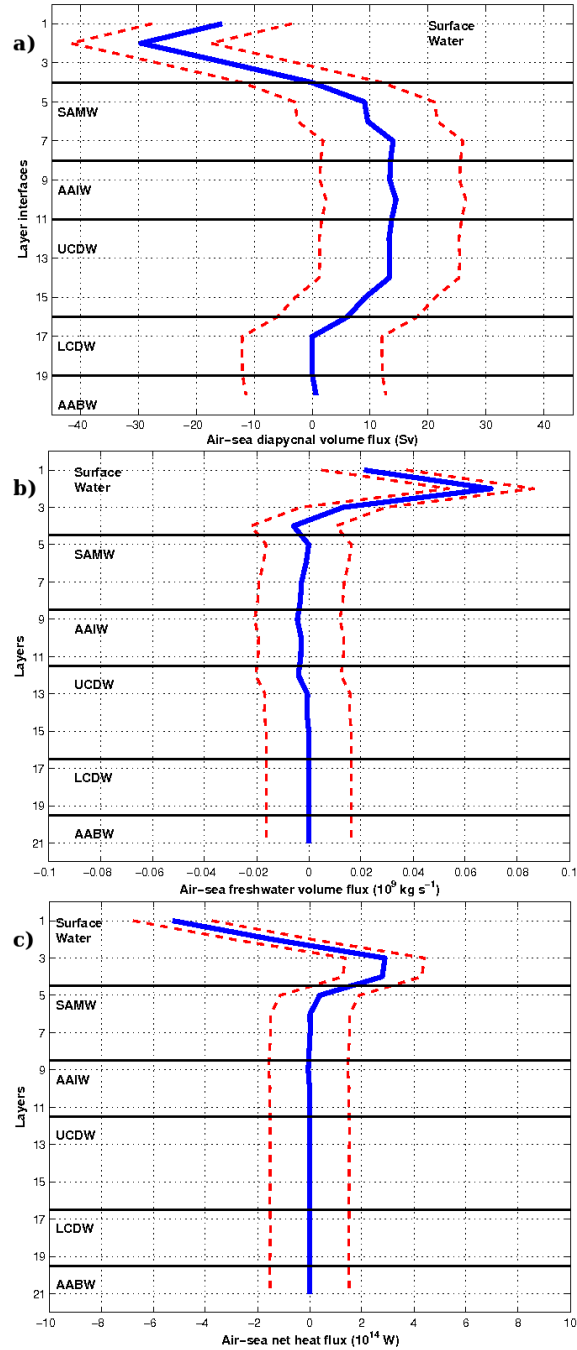


Figure 7: Air-sea interaction induced diapycnal a) volume flux, b) freshwater flux and c) heat flux within the South Atlantic box. Diapycnal volume flux is estimated at the layer interface, freshwater flux and heat flux induced by air-sea interaction is into each individual layer. Positive (negative) values indicate a flux towards lighter (heavier) neutral density classes. Neutral density class boundaries are marked (solid black line), and neutral density classes labelled.

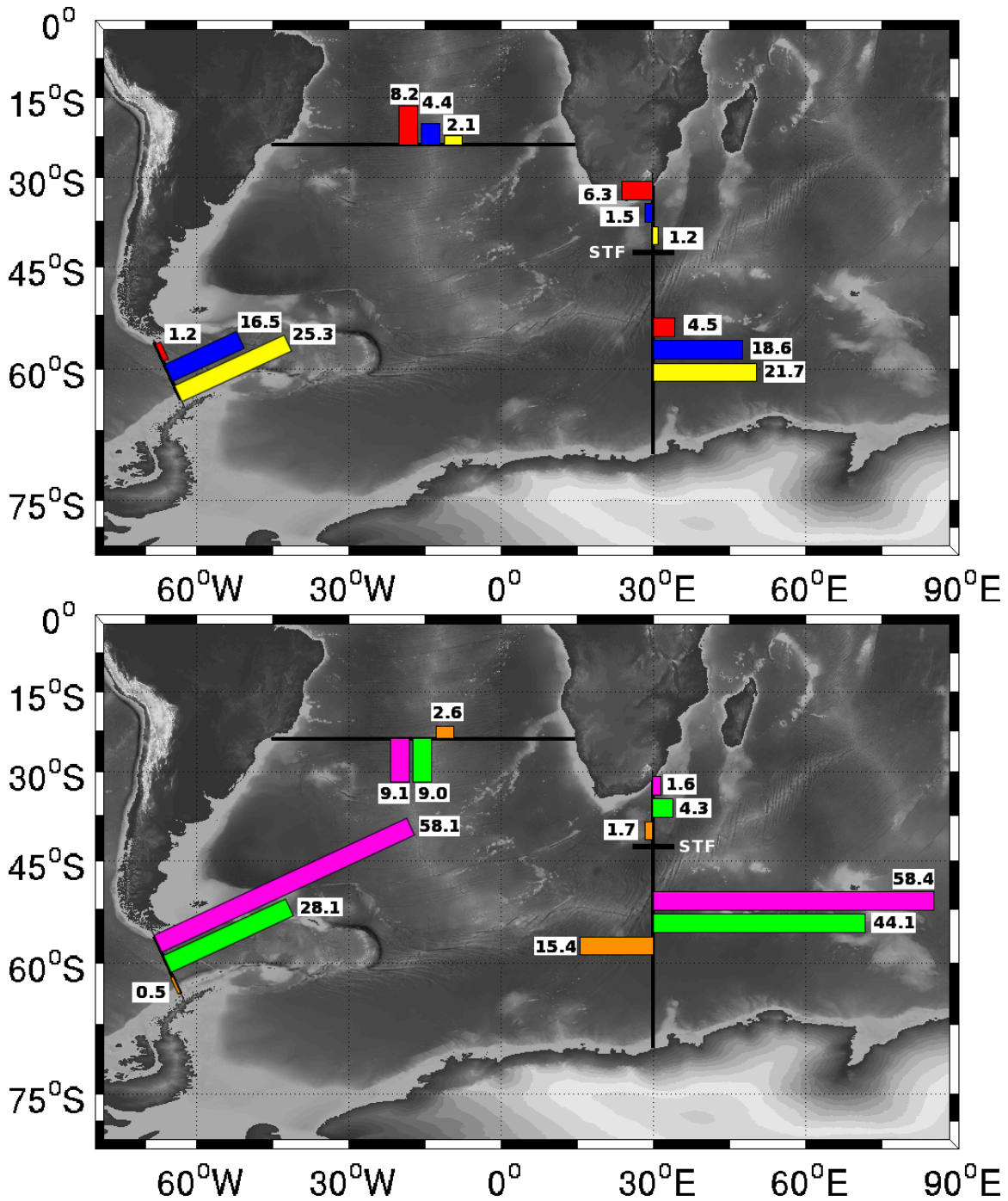


Figure 8: Schematic circulation for the inverse model solution. The length of each bar is proportional to the net transport associated with each neutral density class. Neutral density classes shown are a) surface water (red), SAMW (blue), and AAIW (yellow) and b) UCDW (pink), LCDW (green) and AABW (orange). Numbers at the end of each bar give transports in Sv. A priori uncertainties for transport in each neutral density class

transport are: surface water 4 Sv, SAMW 4 Sv, AAIW 3 Sv, UCDW 2 Sv, LCDW 1 Sv and AABW 0.5 Sv.

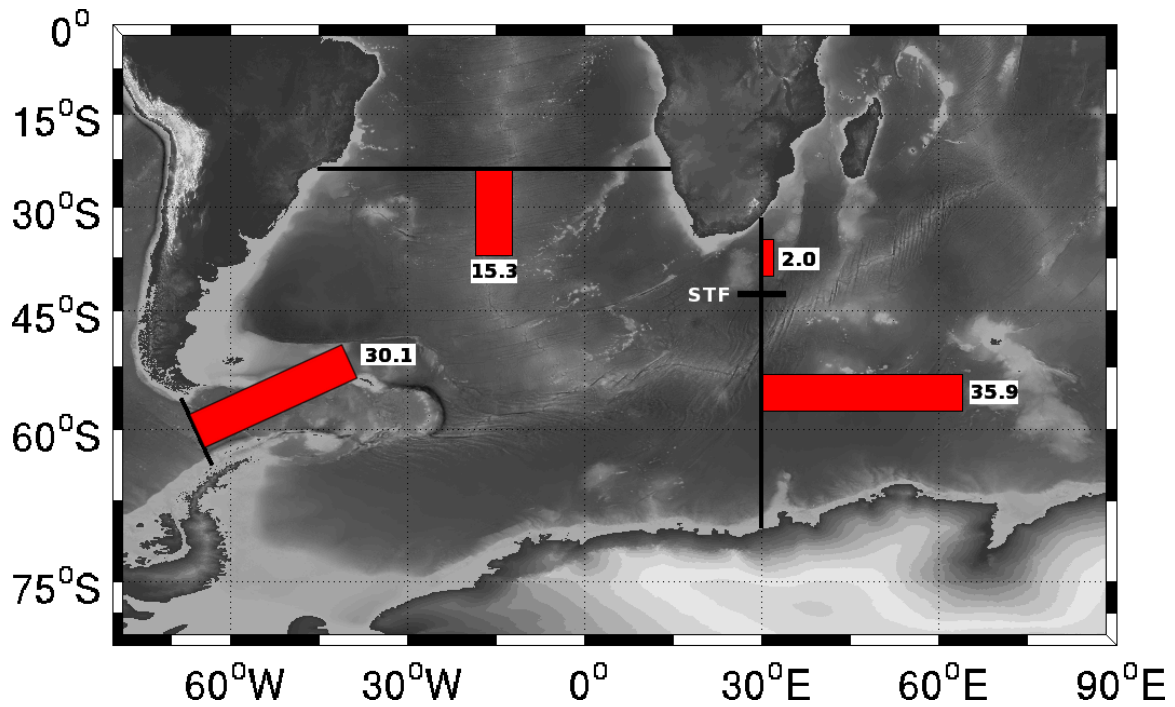


Figure 9: Schematic circulation for the NADW from the inverse model solution, defined as at the UCDW/LCDW interface ($27.90 < \gamma^n < 28.10$), equal to layers 16 and 17 (Table 4). The length of each bar is proportional to the net transport. Numbers at the end of each bar give transports in Sv with an uncertainty of 2 Sv.

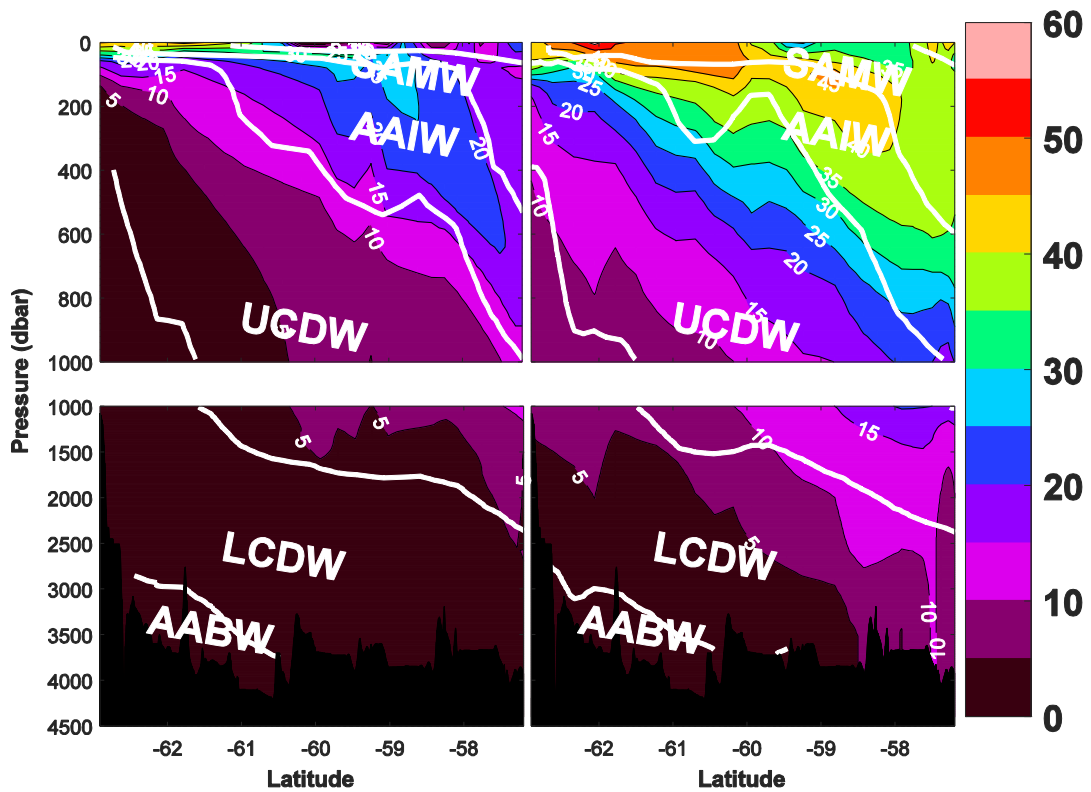


Figure 10: ΔC^* -derived distribution across Drake Passage of C^{ant} for Left: 1990 and Right: 2009. The neutral density:geopotential height interpolation scheme mentioned in Section 2.1 uses a 0.02 geopotential height (φ) grid across Drake Passage. Neutral density classes are labelled following the neutral density interfaces in Table 4. Units of $\mu\text{mol kg}^{-1}$.

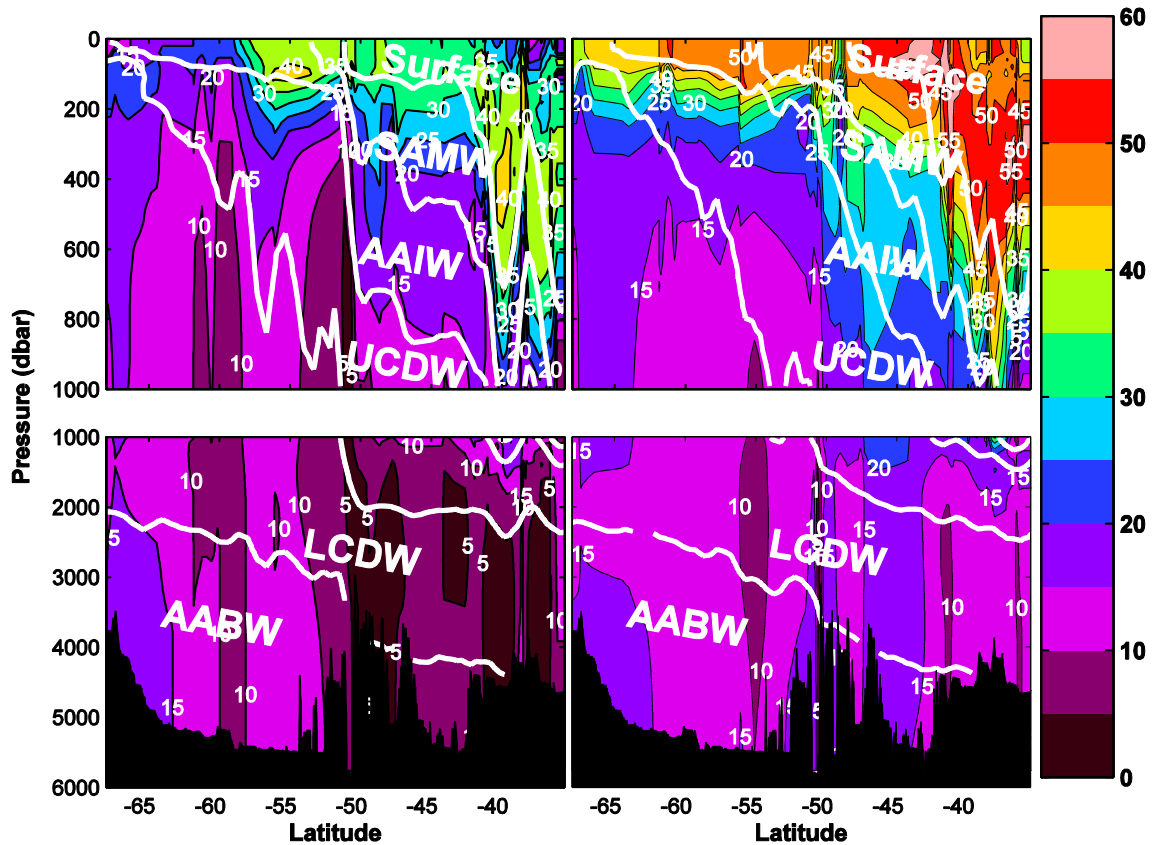


Figure 11: ΔC^* -derived distribution across 30°E of C^{ant} for Left: 1996 and Right: 2008. The neutral density:geopotential height interpolation scheme mentioned in Section 2.1 uses a 0.02 geopotential height (φ) grid across 30°E between 35°S and 58°S and a 0.002 φ grid south of 58°S . Neutral density classes are labelled following the neutral density interfaces in Table 4. Units of $\mu\text{mol kg}^{-1}$.

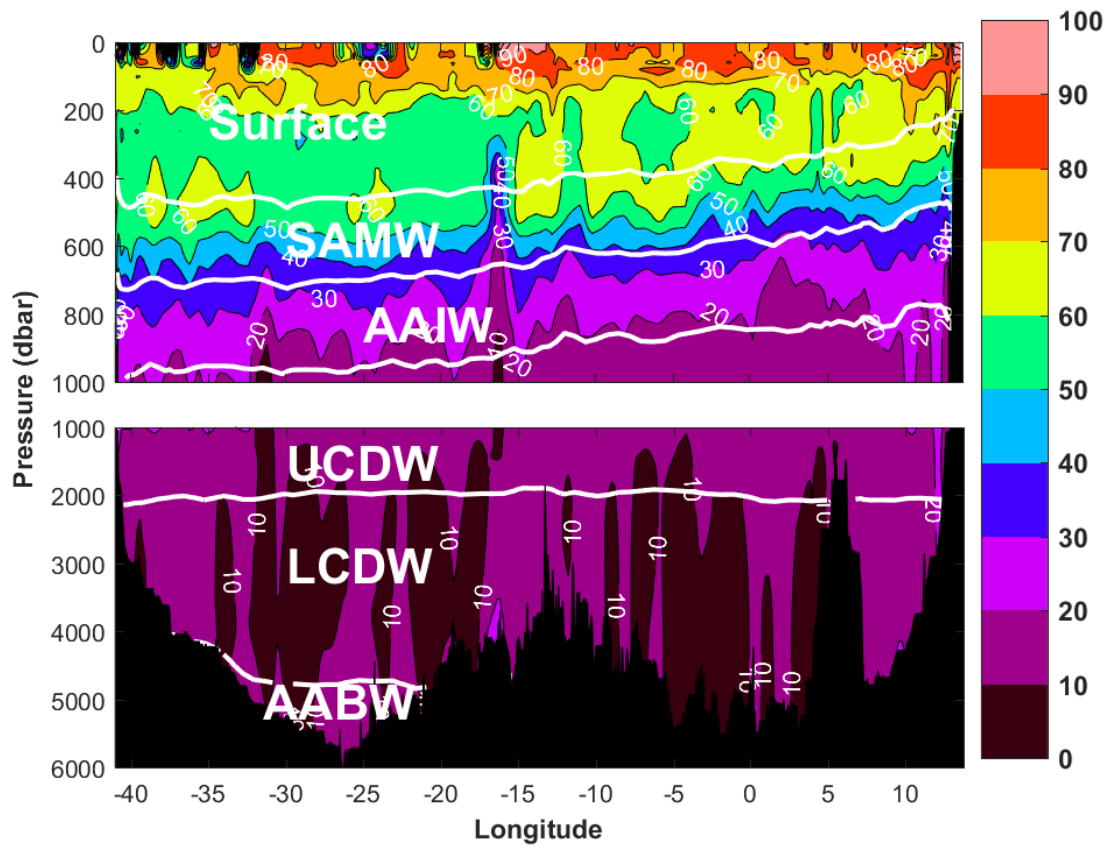


Figure 12: ΔC^* -derived distribution across 24°S of C^{ant} in 2009. Neutral density classes are labelled following the neutral density interfaces in Table 4. Units of $\mu\text{mol kg}^{-1}$.

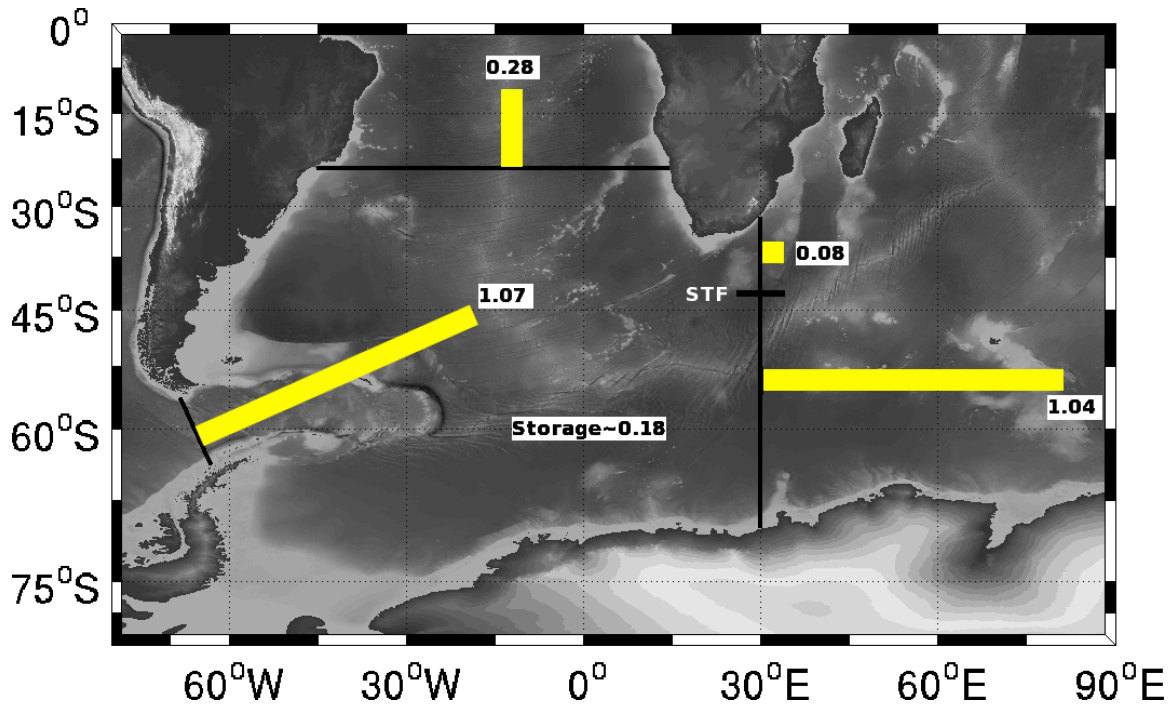


Figure 13: Schematic circulation for the each component of C^{ant} transport within the inverse model solution (PgC yr^{-1}). The length of each bar is proportional to the net transport. The implied net air-sea flux required to maintain the C^{ant} divergence is $0.51 \pm 0.37 \text{ PgC yr}^{-1}$. Numbers at the end of each bar give transports in PgC yr^{-1} . Uncertainties are presented in Table 7.

Table 1: GLODAP/CARINA correction factors as detailed in Gouretski and Jancke (2000), Wanninkhof et al. (2003), Key et al. (2004) and Hoppema et al. (2009). GLODAPv2 correction factors are detailed in Lauvset et al. (2016) and Olsen et al. (2016). Adjustments applied to hydrographic cruises along A13, A14, A15, A16 and A17 are required for section 2.1. Nitrate, phosphate, silicate and alkalinity are in units of $\mu\text{mol kg}^{-1}$. Salinity is listed as an addition in parts per million. Oxygen is listed in units of ml/l requiring multiplication by a factor of 43.55 to convert to $\mu\text{mol kg}^{-1}$ for all cruises apart from A21 (Drake Passage 2009) and 24°S 2008 where the multiplicative factors have already been optimised for $\mu\text{mol kg}^{-1}$.

	Salinity	Nitrate	Phosphate	Oxygen	Silicate	Alkalinity
A21 (Drake Passage 1990)	+1.1	+0.04	-0.06	+0.03	+4.9	$\times 1.0$
A21 (Drake Passage 2009)	$\times 1.0$	$\times 0.975$	$\times 1.0$	$\times 1.035$	$\times 1.0$	-6.0
I6S (30°E 1996)	$\times 1.0$	$\times 0.96$	$\times 0.97$	$\times 1.0$	$\times 0.9$	$\times 1.0$
24°S 2008	$\times 1.0$	$\times 0.99$	$\times 1.0$	$\times 1.035$	$\times 0.95$	$\times 1.0$
A13 (8°E 1995)	+2.8	-1.3	-0.153	+0.003	-3.0	$\times 1.0$
A14 (9°W 1995)	+2.3	-0.19	-0.033	+0.016	-1.9	$\times 1.0$
A15 (19°W 1994)	+0.3	-0.3	-0.023	-0.001	-1.5	$\times 1.0$
A16 (25°W 1989)	-0.5	-0.28	-0.029	+0.019	+0.3	$\times 1.0$
A17 (33°W 1994)	+1.8	+0.06	-0.024	+0.001	+1.6	$\times 1.0$

Table 2: Reference levels for each of the box boundaries. The 30°E section has been split by the Subtropical Front (42.9°S) into an Agulhas and ACC regime.

Section	Reference Level	Reference
Drake Passage	Bottom	Meredith et al., (2011), (King & Jullion, in prep.).
24°S	1300 dbar	Bryden et al., (2011), Warren and Speer, (1991)
30°E Agulhas regime (North of 40°S)	2000 dbar	Arhan et al., (2003; Bryden et al., (2005)
30°E Agulhas regime (40°S – 42.9°S)	Bottom	Arhan et al., (2003)
30°E ACC regime (South of 42.9°S)	Bottom	Park et al., (2001)

Table 3: Constraints applied to better construct the initial field for each of the sections along the box boundary. Positive (negative) values indicate a transport into (out of) the box. The boundary salinity transport refers to the net inflow of salinity transport across Drake Passage, 24°S and the 30°E Agulhas regime combined to equal the net outflow of salinity transport through the ACC regime at 30°E. All constraints are applied to better constrain the initial field. The Ekman transport and the ACC regime boundary salinity transport are not included as explicit constraints within the box inversion. Stated errors are the residual noise terms from the conservation equations.

	Reference	Property	Vertical extent	Constraint	Solution
Drake Passage	Cunningham et al. (2003), Meredith et al. (2011)	Volume	Full depth	136.7±10 Sv	128.4±8.3 Sv
24°S:					
Full section	Coachman and Aagaard, (1988)	Salinity	Full depth	26±0.2 Sv psu	25.8±0.2 Sv psu

Vema and Hunter Channel	Hogg et al. (1999), McDonagh et al. (2002), Zenk et al. (1999)	Volume	$\theta < 2 \text{ }^\circ\text{C}$	$-6.9 \pm 2 \text{ Sv}$	$-6.7 \pm 1.9 \text{ Sv}$
Brazil Current	Bryden et al. (2011)	Volume	Above 300 dbar	$4.9 \pm 5 \text{ Sv}$	$5.8 \pm 0.1 \text{ Sv}$
Cape Basin (East of 6°E)	Arhan et al. (2003), McDonagh and King (2005)	Volume	$\theta < 2 \text{ }^\circ\text{C}$	$0 \pm 1 \text{ Sv}$	$0.2 \pm 0.1 \text{ Sv}$
Ekman transport 30°E:	Bryden et al. (2011)	Volume	Above 80 dbar	3.3 Sv	
Agulhas regime	McDonagh et al. (1999)	Volume	$\theta > 3.5 \text{ }^\circ\text{C}$	$9 \pm 3 \text{ Sv}$	$10.7 \pm 1.3 \text{ Sv}$
ACC regime	This study	Salinity	Full depth	Salinity transport inflow to box (4773.64 Sv psu)	

Table 4: Neutral density limits for each layer and corresponding water classes. Definitions following Orsi et al. (1999), Naveira Garabato et al. (2002a), Heywood and King (2002) and Naveira Garabato et al. (2009). A North Atlantic Deep Water (NADW) neutral density class is labelled at $27.90 < \gamma^n < 28.10$ primarily for usage along the 24 °S section where NADW is prevalent.

Layer	Lower limits	Water classes
1	$\gamma^n < 24$	
2	$24 < \gamma^n < 25$	Surface Water
3	$25 < \gamma^n < 26$	
4	$26 < \gamma^n < 26.80$	
5	$26.80 < \gamma^n < 26.90$	
6	$26.90 < \gamma^n < 27.00$	Subantarctic Mode Water (SAMW)
7	$27.00 < \gamma^n < 27.10$	
8	$27.10 < \gamma^n < 27.23$	
9	$27.23 < \gamma^n < 27.30$	
10	$27.30 < \gamma^n < 27.40$	Antarctic Intermediate Water (AAIW)
11	$27.40 < \gamma^n < 27.50$	
12	$27.50 < \gamma^n < 27.60$	
13	$27.60 < \gamma^n < 27.70$	Upper Circumpolar
14	$27.70 < \gamma^n < 27.80$	Deep Water
15	$27.80 < \gamma^n < 27.90$	(UCDW)
16	$27.90 < \gamma^n < 28.00$	North Atlantic Deep Water
17	$28.00 < \gamma^n < 28.10$	Lower Circumpolar (NADW)
18	$28.10 < \gamma^n < 28.20$	Deep Water
19	$28.20 < \gamma^n < 28.27$	(LCDW)
20	$28.27 < \gamma^n < 28.35$	Antarctic Bottom Water (AABW)
21	$28.35 < \gamma^n$	

Table 5: Meridional property transport from inverse studies and empirical analysis across 24°S, 30°S (WOCE A10) and nominally at 45°S (WOCE A11), adapted from McDonagh and King (2005) and Williams (2007). The MOC strength in this study, is interpreted as the southward flow of deep water, primarily NADW. The MOC strength estimate in Dong et al. (2009) is an average of 17 hydrographic occupations. A northward net flux is positive.

Source	Section	Freshwater (Sv)	Heat (PW)	Salt (Gg s ⁻¹ or Sv psu)	MOC strength (Sv)
Ganachaud (1999)	A11	-	0.66±0.12	-	18±4
Holfort and Siedler (2001)	A11	-0.55±0.02	0.37±0.02	-26.37±0.73	21.7
McDonagh and King (2005)	A11	-0.7	0.43±0.08	-26	21.0±2
Naveira Garabato et al. (2014)	A11	-0.7±0.48	0.14±0.06	-29.2±17.2	15.8
Dong et al. (2009)	35°S	-	0.55±0.14	-	17.9
Rintoul (1991)	32°S	-	0.25	-	-
Lumpkin and Speer (2007)	32°S	-	0.60±0.08	-	-
Ganachaud (1999)	30°S	-	0.35±0.15	-	23±3
Holfort and Siedler (2001)	30°S	-0.51±0.02	0.29±0.05	-26.75±0.77	22.7
Ganachaud and Wunsch (2003)	30°S	-0.5±0.1	-	-26.7	-
McDonagh and King (2005)	30°S	-0.5±0.1	0.22±0.08	-26	19.9±2
Naveira Garabato et al. (2014)	30°S	-0.58±0.48	0.31±0.04	-13.8±17.1	13.7
Bryden et al. (2011)	24°S	-0.34/-0.29	0.7	-26	21.5 / 16.5
This study	24°S	-0.7±0.3	0.40±0.08	-25.8±0.2	20.2±2

Table 6: a) Net heat flux across 24°S separated into overturning and gyre components. b) Overturning component of the salinity transport and associated M_{ov} and M_{az} transports. Positive (negative) transport is defined as northwards (southwards) for compatibility with Bryden et al. (2011).

a)	Overturning (PW)	Gyre (PW)	Total (PW)
This study	0.52	-0.12	0.40
Bryden et al. (2011) 2009 section	0.76	-0.07	0.68
Bryden et al. (2011) 1983 section	0.53	-0.14	0.38

b)	Overturning (Sv psu)	M_{ov} (Sv)	M_{az} (Sv)
This study	3.3	-0.09	0.16
Bryden et al. (2011) 2009 section	4.6	-0.13	0.12
Bryden et al. (2011) 1983 section	3.3	-0.09	0.21

Table 7: C^{ant} transports at the box boundary, C^{ant} storage within the box and C^{ant} air-sea flux in PgC yr^{-1} . Positive (negative) values indicate a transport into (out of) the box.

Section	C^{ant} Transport (Pg C yr^{-1})
Drake Passage	+1.07±0.44
24°S	-0.28±0.16
30°E: Agulhas	-0.08±0.07
30°E: ACC	-1.04±0.42
Total	-0.33±0.31
Storage	+0.18±0.12
Air-Sea flux	+0.51±0.37

Table 8: Transport-weighted C^{ant} ($\mu\text{mol kg}^{-1}$) at each box boundary. For 24°S and 30°E (Agulhas), the transports are separated into north-south, or east-west components respectively, given the substantial flow in both directions. Uncertainties are the standard error of the mean with units of $\mu\text{mol kg}^{-1}$.

Neutral density	Drake Passage	24°S		30°E (Agulhas)		30°E
		North	South	West	East	
Surface	34.9±0.4	65.2±0.3	63.2±0.4	48.2±0.3	49.7±0.2	50.0±0.5
SAMW	39.2±0.3	51.9±0.4	50.8±0.4	29.2±0.6	35.6±0.7	40.9±0.6
AAIW	36.0±0.5	26.9±0.3	25.8±0.3	16.8±0.5	17.8±0.4	31.8±0.5
UCDW	16.3±0.2	14.3±0.1	13.9±0.1	16.5±0.1	16.3±0.1	16.6±0.2
LCDW	6.9±0.1	10.2±0.1	10.8±0.1	11.1±0.1	12.6±0.1	10.3±0.1
AABW	2.2±0.1	12.6±0.2	11.1±0.2	10.1±0.1	11.7±0.1	11.1±0.1
Total	20.9±0.2	30.1±0.2	25.6±0.2	33.8±0.3	35.1±0.3	18.8±0.1

Table 9: Mean Penetration Depth (MPD), mean $\Delta C_{\text{ml}}^{\text{ant}}$ ($\mu\text{mol kg}^{-1} \text{yr}^{-1}$) within mixed layer and mean in-situ density ρ_{ml} (kg m^{-3}) within mixed layer for Drake Passage, 30°E, and 24°S and a mean of the hydrographic sections. Along 30°E, C^{ant} is normalised to a mean temperature. MPD is estimated to have a 20% uncertainty, and a $\pm 0.5 \mu\text{mol kg}^{-1} \text{yr}^{-1}$ $\Delta C_{\text{ml}}^{\text{ant}}$ uncertainty.

	MPD (m)	$\Delta C_{\text{ml}}^{\text{ant}}$ ($\mu\text{mol kg}^{-1} \text{yr}^{-1}$)	ρ_{ml} (kg m^{-3})
Drake Passage	259.8	0.84	1027.0
24°S	933.2	0.85	1024.8
30°E	624.3	0.45	1026.2
Mean	605.8	0.71	1025.9

Table 10: Comparison of C^{ant} storage rate ($\text{mol m}^{-2} \text{yr}^{-1}$) for the South Atlantic (south of 15°S), and South Atlantic sector of the Southern Ocean. For Peng and Wanninkhof (2010), the two estimates derive from two different calculation methods.

Author	Region	Storage rate ($\text{mol m}^{-2} \text{yr}^{-1}$)
Holfort et al. (1998)	10°S -30°S	0.59±0.12
Murata et al. (2008)	Along 30°S	0.6±0.1
Peng and Wanninkhof (2010)	South of 15°S	0.56/0.35±0.3
Wanninkhof et al. (2010)	South of 15°S	0.76
Ríos et al. (2012)	10°N-55°S, western basin	0.92±0.13
This study	Drake Passage	0.22±0.29
This study	24°S	0.81±0.53
This study	30°E	0.29±0.18
This study	Mean	0.44±0.30

References

- Adler, R.F., Huffman, G.J., Chang, A., Ferraro, R., Xie, P.-P., Janowiak, J., Rudolf, B., Schneider, U., Curtis, S., Bolvin, D., Gruber, A., Susskind, J., Arkin, P., Nelkin, E., 2003. The Version-2 Global Precipitation Climatology Project (GPCP) Monthly Precipitation Analysis (1979 – Present). *J. Hydrometeorol.* 4, 1147–1167.
- Álvarez, M., Ríos, A.F., Pérez, F.F., Bryden, H.L., Rosón, G., 2003. Transports and budgets of total inorganic carbon in the subpolar and temperate North Atlantic. *Global Biogeochem. Cycles* 17, 1–22. doi:10.1029/2002GB001881
- Antonov, J.I., Seidov, D., Boyer, T.P., Locarnini, R.A., Mishonov, A. V., Garcia, H.E., Baranova, O.K., Zweng, M.M., Johnson, D.R., 2010. *World Ocean Atlas 2009, Volume 2: Salinity*. Washington, D.C.
- Arhan, M., Mercier, H., Park, Y.-H., 2003. On the deep water circulation of the eastern South Atlantic Ocean. *Deep Sea Res. Part I Oceanogr. Res. Pap.* 50, 889–916. doi:10.1016/S0967-0637(03)00072-4
- Beal, L.M., Bryden, H.L., 1999. The velocity and vorticity structure of the Agulhas Current at 32°S. *J. Geophys. Res.* 104, 5151–5176. doi:10.1029/1998JC900056
- Belkin, I.M., Gordon, A.L., 1996. Southern Ocean fronts from the Greenwich meridian to Tasmania. *J. Geophys. Res.* 101, 3675–3696. doi:10.1029/95JC02750
- Berry, D.I., Kent, E.C., 2009. A New Air–Sea Interaction Gridded Dataset from ICOADS With Uncertainty Estimates. *Bull. Am. Meteorol. Soc.* 90, 645–656. doi:10.1175/2008BAMS2639.1
- Berry, D.I., Kent, E.C., 2011. Air-Sea fluxes from ICOADS: the construction of a new gridded dataset with uncertainty estimates. *Int. J. Climatol.* 31, 987–1001. doi:10.1002/joc.2059
- Boyer, T., Levitus, S., Garcia, H., Locarnini, R.A., Stephens, C., Antonov, J., 2005. Objective analyses of annual, seasonal, and monthly temperature and salinity for the World Ocean on a 0.25° grid. *Int. J. Climatol.* 25, 931–945. doi:10.1002/joc.1173
- Brewer, P.G., 1978. Direct observation of the oceanic CO₂ increase. *Geophys. Res. Lett.* 5, 997–1000.
- Brewer, P.G., Wong, G.T.F., Bacon, M.P., Spencer, D.W., 1975. An Oceanic Calcium Problem. *Earth Planet. Sci. Lett.* 26, 81–87.
- Broecker, W.S., Takahashi, T., Simpson, H.J., Peng, T.-H., 1979. Fate of fossil fuel carbon dioxide and the global carbon budget. *Science.* 206, 409–418. doi:10.1126/science.206.4417.409
- Brown, P.J., Jullion, L., Landschützer, P., Bakker, D.C.E., Naveira Garabato, A.C., Meredith, M.P., Torres-Valdés, S., Watson, A.J., Hoppema, M., Loose, B., Jones, E.M., Telszewski, M., Jones, S.D., Wanninkhof, R., 2015. Carbon dynamics of the Weddell Gyre, Southern Ocean. *Global Biogeochem. Cycles* 29, 288–306. doi:10.1002/2014GB005006.Received

- Brunke, M.A., Wang, Z., Zeng, X., Bosilovich, M., Shie, C.-L., 2011. An Assessment of the Uncertainties in Ocean Surface Turbulent Fluxes in 11 Reanalysis, Satellite-Derived, and Combined Global Datasets. *J. Clim.* 24, 5469–5493. doi:10.1175/2011JCLI4223.1
- Bryden, H.L., Beal, L.M., Duncan, L.M., 2005. Structure and Transport of the Agulhas Current and Its Temporal Variability. *J. Oceanogr.* 61, 479–492. doi:10.1007/s10872-005-0057-8
- Bryden, H.L., Imawaki, S., 2001. Ocean heat transport, in: Siedler, G., Church, J., Gould, J. (Eds.), *Ocean Circulation and Climate*. Academic Press, pp. 455–474.
- Bryden, H.L., King, B.A., McCarthy, G.D., 2011. South Atlantic overturning circulation at 24 ° S. *J. Mar. Res.* 39–56.
- Casal, T.G.D., Beal, L.M., Lumpkin, R., Johns, W.E., 2009. Structure and downstream evolution of the Agulhas Current system during a quasi-synoptic survey in February–March 2003. *J. Geophys. Res.* 114, C03001. doi:10.1029/2008JC004954
- Chen, G.-T., Millero, F.J., 1979. Gradual increase of oceanic CO₂. *Nature* 277, 205–206.
- Cimatoribus, A.A., Drijfhout, S.S., Toom, M., Dijkstra, H.A., 2012. Sensitivity of the Atlantic meridional overturning circulation to South Atlantic freshwater anomalies. *Clim. Dyn.* 39, 2291–2306. doi:10.1007/s00382-012-1292-5
- Cisewski, B., Strass, V.H., Leach, H., 2011. Circulation and transport of water masses in the Lazarev Sea, Antarctica, during summer and winter 2006. *Deep Sea Res. Part I Oceanogr. Res. Pap.* 58, 186–199. doi:10.1016/j.dsr.2010.12.001
- Coachman, L.K., Aagaard, K., 1988. Transports Through Bering Strait: Annual and Interannual Variability. *J. Geophys. Res.* 93, 15535–15539. doi:10.1029/JC093iC12p15535
- Culberson, C.H., Huang, S., 1987. Automated amperometric oxygen titration. *Deep Sea Res. Part A. Oceanogr. Res. Pap.* 34, 875–880. doi:10.1016/0198-0149(87)90042-2
- Culberson, C.H., Knapp, G., Stalcup, M., Williams, R.T., Zemylak, F., 1991. A comparison of methods for the determination of dissolved oxygen in seawater. Report WHPO 91-92.
- Cunningham, S.A., Alderson, S.G., King, B.A., Brandon, M.A., 2003. Transport and variability of the Antarctic Circumpolar Current in Drake Passage. *J. Geophys. Res.* 108, 8084. doi:10.1029/2001JC001147
- Dencausse, G., Arhan, M., Speich, S., 2010. Spatio-temporal characteristics of the Agulhas Current retroflexion. *Deep Sea Res. Part I Oceanogr. Res. Pap.* 57, 1392–1405. doi:10.1016/j.dsr.2010.07.004
- DeVries, T., 2014. The oceanic anthropogenic CO₂ sink: Storage, air-sea fluxes, and transports over the industrial era. *Global Biogeochem. Cycles* 28, 631–647. doi:10.1002/2013GB004739
- Dickson, A.G., Afghan, J.D., Anderson, G.C., 2003. Reference materials for oceanic CO₂

- analysis: a method for the certification of total alkalinity. *Mar. Chem.* 80, 185–197. doi:10.1016/S0304-4203(02)00133-0
- Dickson, A.G., Sabine, C.L., Christian, J.R., 2007. Guide to best practices for ocean CO₂ measurements. *PICES Spec. Publ.* 3, 1991.
- Dijkstra, H.A., 2007. Characterization of the multiple equilibria regime in a global ocean model. *Tellus A* 59, 695–705. doi:10.1111/j.1600-0870.2007.00267.x
- Dong, J., Speer, K.G., Jullion, L., 2016. The Antarctic Slope Current near 30°E. *J. Geophys. Res. Ocean.* 121, 1051–1062. doi:10.1002/2015JC011099
- Dong, S., Garzoli, S., Baringer, M., Meinen, C., Goni, G., 2009. Interannual variations in the Atlantic meridional overturning circulation and its relationship with the net northward heat transport in the South Atlantic. *Geophys. Res. Lett.* 36, L20606. doi:10.1029/2009GL039356
- Evans, D.L., Signorini, S.R., 1985. Vertical Structure of the Brazil Current. *Nature* 315, 48–50.
- Evans, D.L., Signorini, S.R., Miranda, L.B., 1983. A Note on the Transport of the Brazil Current. *J. Phys. Oceanogr.* 13, 1732–1738.
- Evans, G.R., 2013. A study of the South Atlantic Ocean: Circulation and Carbon Variability. Ph.D. Thesis. University of Southampton, 389 pp. <http://eprints.soton.ac.uk/id/eprint/359128>.
- Fahrbach, E., Rohardt, G., Scheele, N., Schröder, M., Strass, V., Wisotzki, A., 1995. Formation and discharge of deep and bottom water in the northwestern Weddell Sea. *J. Mar. Res.* 53, 515–538.
- Fofonoff, N.P., Millard, R.C., 1983. Algorithms for computation of fundamental properties of seawater. *Unesco Tech. Pap. Mar. Sci.* 44.
- Fraga, F., Álvarez-Salgado, X.A., 2005. On the variation of alkalinity during phytoplankton photosynthesis. *Ciencias Mar.* 31, 627–639.
- Gammon, R.H., Cline, J., Wisegarver, D., 1982. Chlorofluoromethanes in the Northeast Pacific Ocean: Measured Vertical Distributions and Application as Transient Tracers of Upper and Ocean Mixing. *J. Geophys. Res.* 87, 9441–9454.
- Ganachaud, A., Wunsch, C., 2003. Large-Scale Ocean Heat and Freshwater Transports during the World Ocean Circulation Experiment. *J. Clim.* 16, 696–705. doi:10.1175/1520-0442(2003)016<0696:LSOHAF>2.0.CO;2
- Ganachaud, A.S., 1999. Large Scale Oceanic Circulation and Fluxes of Freshwater, Heat, Nutrients and Oxygen. Ph.D. Thesis. Massachusetts Institute of Technology/Woods Hole Oceanographic Institution Joint Program, 267 pp.
- Ganachaud, A.S., 2003. Error Budget of Inverse Box Models : The North Atlantic. *J. Atmos. Ocean. Technol.* 20, 1641–1655.
- Garfield, N.I., 1990. The Brazil Current at Subtropical Latitudes. Ph.D. Thesis. University of Rhode Island, Providence, 121 pp.

- Garzoli, S.L., Gordon, A.L., 1996. Origins and variability of the Benguela Current. *J. Geophys. Res.* 101, 897–906.
- Georgi, D.T., Toole, J.M., 1982. The Antarctic Circumpolar Current and the oceanic heat and freshwater budgets. *J. Mar. Res.* 40, Supplement, 183-197.
- Gladyshev, S., Arhan, M., Sokov, A., Speich, S., 2008. A hydrographic section from South Africa to the southern limit of the Antarctic Circumpolar Current at the Greenwich meridian. *Deep Sea Res. Part I Oceanogr. Res. Pap.* 55, 1284–1303. doi:10.1016/j.dsr.2008.05.009
- Gloor, M., Gruber, N., Sarmiento, J., Sabine, C.L., Feely, R.A., Rodenbeck, C., 2003. A first estimate of present and preindustrial air-sea CO₂ flux patterns based on ocean interior carbon measurements and models. *Geophys. Res. Lett.* 30, L01010, doi:10.1029/2002GL015594. doi:10.1029/2002GL015594
- Gordon, A.L., 1986. Interocean Exchange of Thermocline Water. *J. Geophys. Res.* 91, 5037–5046. doi:10.1029/JC091iC04p05037
- Gordon, A.L., Greengrove, C.L., 1986. Geostrophic circulation of the Brazil-Falkland confluence. *Deep Sea Res.* 33, 573–585.
- Gordon, A.L., Huber, B., McKee, D., Visbeck, M., 2010. A seasonal cycle in the export of bottom water from the Weddell Sea. *Nat. Geosci.* 3, 551–556. doi:10.1038/ngeo916
- Gordon, L.I., Jennings, J.C., Ross, A.A., Krest, J.M., 1993. A Suggested Protocol for Continuous Flow Automated Analysis of Seawater Nutrients (Phosphate, Nitrate, Nitrite and Silicic Acid) in the WOCE Hydrographic Program and the Joint Global Ocean Fluxes Study. *WOCE Oper. Man. Part 3* 1–55.
- Gouretski, V., Jancke, K., 2000. Systematic errors as the cause for an apparent deep water property variability: global analysis of the WOCE and historical hydrographic data. *Prog. Oceanogr.* 48, 337–402. doi:10.1016/S0079-6611(00)00049-5
- Gouretski, V. V., Koltermann, K.P., 2004. WOCE Global Hydrographic climatology. *Berichte des Bundesamtes für Seeschifffahrt und Hydrogr.* 35, 1–52.
- Grist, J.P., Josey, S.A., 2003. Inverse Analysis Adjustment of the SOC Air – Sea Flux Climatology Using Ocean Heat Transport Constraints. *J. Clim.* 16, 3274–3295.
- Gruber, N., Gloor, M., Mikaloff Fletcher, S.E., Doney, S.C., Dutkiewicz, S., Follows, M.J., Gerber, M., Jacobson, A.R., Joos, F., Lindsay, K., Menemenlis, D., Mouchet, A., Muller, S.A., Sarmiento, J.L., Takahashi, T., 2009. Oceanic sources, sinks, and transport of atmospheric CO₂. *Global Biogeochem. Cycles* 23, GB1005. doi:10.1029/2008GB003349
- Gruber, N., Sarmiento, J.L., Stocker, T.F., 1996. An improved method for detecting anthropogenic CO₂ in the oceans. *Global Biogeochem. Cycles* 10, 809–837.
- Hall, M.M., Bryden, H.L., 1982. Direct estimates and mechanisms of ocean heat transport. *Deep Sea Res.* 29, 339–359.

- Heywood, K.J., King, B.A., 2002. Water masses and baroclinic transports in the South Atlantic and Southern oceans. *J. Mar. Res.* 60, 639–676. doi:10.1357/002224002762688687
- Heywood, K.J., Naveira Garabato, A.C., Stevens, D.P., 2002. High mixing rates in the abyssal Southern Ocean. *Nature* 415, 1011–4. doi:10.1038/4151011a
- Hogg, N.G., Siedler, G., Zenk, W., 1999. Circulation and Variability at the Southern Boundary of the Brazil Basin. *J. Phys. Oceanogr.* 29, 145–157. doi:10.1175/1520-0485(1999)029<0145:CAVATS>2.0.CO;2
- Holfort, J., Johnson, K.M., Schneider, B., Siedler, G., Wallace, D.W.R., 1998. Meridional transport of dissolved inorganic carbon. *Global Biogeochem. Cycles* 12, 479–499.
- Holfort, J., Siedler, G., 2001. The Meridional Oceanic Transports of Heat and Nutrients in the South Atlantic. *J. Phys. Oceanogr.* 31, 5–29. doi:10.1175/1520-0485(2001)031<0005:TMOTOH>2.0.CO;2
- Hoppema, M., Velo, A., van Heuven, S., Tanhua, T., Key, R.M., Lin, X., Bakker, D.C.E., Perez, F.F., 2009. Consistency of cruise data of the CARINA database in the Atlantic sector of the Southern Ocean. *Earth Syst. Sci. Data* 63–75. doi:10.3334/CDIAC/otg.CARINA.SO.V1.0
- Huhn, O., Rhein, M., Hoppema, M., van Heuven, S., 2013. Decline of deep and bottom water ventilation and slowing down of anthropogenic carbon storage in the Weddell Sea, 1984–2011. *Deep. Res. Part I Oceanogr. Res. Pap.* 76, 66–84. doi:10.1016/j.dsr.2013.01.005
- Huisman, S.E., den Toom, M., Dijkstra, H.A., Drijfhout, S., 2010. An Indicator of the Multiple Equilibria Regime of the Atlantic Meridional Overturning Circulation. *J. Phys. Oceanogr.* 40, 551–567. doi:10.1175/2009JPO4215.1
- Iudicone, D., Rodgers, K.B., Stendardo, I., Aumont, O., Madec, G., Bopp, L., Mangoni, O., Ribera D'Alcala', M., 2011. Water masses as a unifying framework for understanding the Southern Ocean Carbon Cycle. *Biogeosciences* 8, 1031–1052. doi:10.5194/bg-8-1031-2011
- Jackett, D.R., McDougall, T.J., 1997. A Neutral Density Variable for the World's Oceans. *J. Phys. Oceanogr.* 27, 237–263. doi:10.1175/1520-0485(1997)027<0237:ANDVFT>2.0.CO;2
- Jacobs, S.S., 1991. On the nature and significance of the Antarctic Slope Front. *Mar. Chem.* 35, 9–24. doi:10.1016/S0304-4203(09)90005-6
- Jacobson, A.R., Mikaloff Fletcher, S.E., Gruber, N., Sarmiento, J.L., Gloor, M., 2007. A joint atmosphere-ocean inversion for surface fluxes of carbon dioxide: 1. Methods and global-scale fluxes. *Global Biogeochem. Cycles* 21. doi:10.1029/2005GB002556
- Johnson, A., Biscaye, E., 1976. Abyssal Hydrography, Nephelometry, Currents, and Benthic Boundary Layer Structure in the Vema Channel. *J. Geophys. Res.* 81, 5771–5786.

- Johnson, K.M., King, A.E., Sieburth, J.M., 1985. Coulometric TCO₂ Analyses for Marine Studies; An Introduction. *Mar. Chem.* 16, 61–82.
- Johnson, K.M., Sieburth, J.M., Williams, P.J. leB., Brändström, L., 1987. Coulometric Total Carbon Dioxide Analysis for Marine Studies: Automation and Calibration. *Mar. Chem.* 21, 117–133.
- Johnson, K.M., Wallace, D.W.R., 1992. The Single-Operator Multiparameter Metabolic Analyzer for total carbon dioxide with coulometric detection. *DOE Res. Summ.* 19, 1–4.
- Johnson, K.M., Wills, K.D., Butler, D.B., Johnson, W.K., Wong, C.S., 1993. Coulometric total carbon dioxide analysis for marine studies : maximizing the performance of an automated gas extraction system and coulometric detector. *Mar. Chem.* 44, 167–187.
- Jullion, L., Heywood, K.J., Naveira Garabato, A.C., Stevens, D.P., 2010a. Circulation and Water Mass Modification in the Brazil–Malvinas Confluence. *J. Phys. Oceanogr.* 40, 845–864. doi:10.1175/2009JPO4174.1
- Jullion, L., Jones, S.C., Naveira Garabato, A.C., Meredith, M.P., 2010b. Wind-controlled export of Antarctic Bottom Water from the Weddell Sea. *Geophys. Res. Lett.* 37, L09609. doi:10.1029/2010GL042822
- Jullion, L., Naveira Garabato, A.C., Bacon, S., Meredith, M.P., Brown, P.J., Torres-Valdés, S., Speer, K.G., Holland, P.J., Dong, J., Bakker, D.C.E., Hoppema, M., Loose, B., Venables, H.J., Jenkins, W.J., Messias, M.-J., Fahrbach, E., 2014. The contribution of the Weddell Gyre to the lower limb of the Global Overturning Circulation. *J. Geophys. Res. Ocean.* 119, 3357–3377. doi:10.1002/2013JC009725
- Karstensen, J., Tomczak, M., 1998. Age determination of mixed water masses using CFC and oxygen data. *J. Geophys. Res.* 103, 18599–18609.
- Key, R.M., Kozyr, A., Sabine, C.L., Lee, K., Wanninkhof, R., Bullister, J.L., Feely, R.A., Millero, F.J., Mordy, C., Peng, T.-H., 2004. A global ocean carbon climatology: Results from Global Data Analysis Project (GLODAP). *Global Biogeochem. Cycles* 18, GB4031, doi:10.1029/2004GB002247. doi:10.1029/2004GB002247
- Key, R.M., Tanhua, T., Olsen, A., Hoppema, M., Jutterström, S., Schirnack, C., van Heuven, S., Kozyr, A., Lin, X., Velo, A., Wallace, D.W.R., Mintrop, L., 2010. The CARINA data synthesis project: introduction and overview. *Earth Syst. Sci. Data* 2, 105–121.
- Khaliwala, S., Tanhua, T., Mikaloff Fletcher, S., Gerber, M., Doney, S.C., Graven, H.D., Gruber, N., McKinley, G.A., Murata, A., Ríos, A.F., Sabine, C.L., Sarmiento, J.L., 2013. Global ocean storage of anthropogenic carbon. *Biogeosciences* 10, 2169–2191. doi:10.5194/bgd-9-8931-2012
- King, B.A., 2010. A095 Cruise Report: Hydrographic sections across the Brazil Current and at 24°S in the Atlantic, RRS James Cook, 740H20090307, Tech. Rep., cchdo.ucsd.edu/data/a095_740H20090307do.pdf.

- Kirkwood, D., 1996. Nutrients : Practical notes on their determination in sea water. ICES Tech. Mar. Environ. Sci. Copenhagen, International Council for the Explorat.
- Lachkar, Z., Orr, J.C., Dutay, J.-C., 2009. Seasonal and mesoscale variability of oceanic transport of anthropogenic CO₂. *Biogeosciences* 6, 2509–2523.
- Lauvset, S.K., Key, R.M., Olsen, A., van Heuven, S., Velo, A., Lin, X., Schirnick, C., Kozyr, A., Tanhua, T., Hoppema, M., Jutterström, S., Steinfeldt, R., Jeansson, E., Ishii, M., Perez, F.F., Suzuki, T., Watelet, S., 2016. A new global interior ocean mapped climatology: the 1° x 1° GLODAP version 2. *Earth Syst. Sci. Data Discuss.* doi:10.5194/essd-2015-42
- Legeais, J.-F., Speich, S., Arhan, M., Ansorge, I., Fahrbach, E., Garzoli, S., Klepikov, A., 2005. The baroclinic transport of the Antarctic Circumpolar Current south of Africa. *Geophys. Res. Lett.* 32, L2460. doi:10.1029/2005GL023271
- Lenton, A., Tilbrook, B., Law, R.M., Bakker, D., Doney, S.C., Gruber, N., Ishii, M., Hoppema, M., Lovenduski, N.S., Matear, R.J., McNeil, B.I., Metzl, N., Mikaloff Fletcher, S.E., Monteiro, P.M.S., Rödenbeck, C., Sweeney, C., Takahashi, T., 2013. Sea–air CO₂ fluxes in the Southern Ocean for the period 1990–2009. *Biogeosciences* 10, 4037–4054. doi:10.5194/bg-10-4037-2013
- Lewis, E., Wallace, D.W.R., 1998. Program developed for CO₂ system calculations. Rep. ORNL/CDIAC-105 Carbon Dioxide Information Analysis Center, Oak Ri.
- Liu, J., Xiao, T., Chen, L., 2011. Intercomparisons of Air–Sea Heat Fluxes over the Southern Ocean. *J. Clim.* 24, 1198–1211. doi:10.1175/2010JCLI3699.1
- Locarini, R.A., Mishonov, A. V., Antonov, J.I., Boyer, T.P., Garcia, H.E., Baranova, O.K., Zweng, M.M., Johnson, D.R., 2010. *World Ocean Atlas 2009, Volume 1: Temperature*. Washington, D.C.
- Locarnini, R.A., Whitworth, T., Nowlin, W.D., 1993. The importance of the Scotia Sea on the outflow of Weddell Sea Deep Water. *J. Mar. Res.* 51, 135–153.
- Lumpkin, R., Speer, K., 2007. Global Ocean Meridional Overturning. *J. Phys. Oceanogr.* 37, 2550. doi:10.1175/JPO3130.1
- Lutjeharms, J.R.E., Van Ballegooyen, R.C., 1988. The Retroflection of the Agulhas Current. *J. Phys. Oceanogr.* 18, 1570–1583.
- Marshall, J., Speer, K., 2012. Closure of the meridional overturning circulation through Southern Ocean upwelling. *Nat. Geosci.* 5, 171–180. doi:10.1038/ngeo1391
- Matano, R.P., Simionato, C.G., de Ruijter, W.P., van Leeuwen, P.J., Strub, P.T., Chelton, D.B., Schlax, M.G., 1998. Seasonal variability in the Agulhas Retroflection region. *Geophys. Res. Lett.* 25, 4361–4364.
- McDonagh, E., Arhan, M., Heywood, K., 2002. On the circulation of bottom water in the region of the Vema Channel. *Deep Sea Res. Part I Oceanogr. Res. Pap.* 49, 1119–1139. doi:10.1016/S0967-0637(02)00016-X
- McDonagh, E.L., 2009. JC031/SR01 Cruise Report: Hydrographic sections of Drake

Passage, RRS James Cook, 740H20090203, Tech. Rep.,
cchdo.ucsd.edu/data/2835/sr01_740H20090203do.pdf.

- McDonagh, E.L., Heywood, K.J., Meredith, M.P., 1999. On the structure, paths, and fluxes associated with Agulhas rings. *J. Geophys. Res.* 104, 7–20.
- McDonagh, E.L., King, B.A., 2005. Oceanic Fluxes in the South Atlantic. *J. Phys. Oceanogr.* 35, 109. doi:10.1175/JPO-2666.1
- McIntosh, P.C., Rintoul, S.R., 1997. Do Box Inverse Models Work? *J. Phys. Oceanogr.* 27, 291–308. doi:10.1175/1520-0485(1997)027<0291:DBIMW>2.0.CO;2
- Meijers, A.J.S., Klocker, A., Bindoff, N.L., Williams, G.D., Marsland, S.J., 2010. The circulation and water masses of the Antarctic shelf and continental slope between 30 and 80°E. *Deep Sea Res. Part II Top. Stud. Oceanogr.* 57, 723–737. doi:10.1016/j.dsr2.2009.04.019
- Mémery, L., 1994. A17 Cruise Report: Maurice Ewing, 35A3CITHER3_2, Tech Rep., cchdo.uscd.edu/data/2171/a17do.pdf.
- Mercier, H., Arhan, M., 1995. A13/A14 Cruise Report: L'Atalante, 35A3CITHER3_1/35A3CITHER3_2, Tech. Rep, cdiac.ornl.gov/ftp/oceans/a14a13woce/a14_35A3CITHER3_1do.pdf.
- Mercier, H., Arhan, M., Lutjeharms, J., 2003. Upper-layer circulation in the eastern Equatorial and South Atlantic Ocean in January–March 1995. *Deep Sea Res. Part I Oceanogr. Res. Pap.* 50, 863–887. doi:10.1016/S0967-0637(03)00071-2
- Meredith, M.P., 2013. Oceanography: Replenishing the abyss. *Nat. Geosci.* 6, 166–167. doi:10.1038/ngeo1743
- Meredith, M.P., Woodworth, P.L., Chereskin, T.K., Marshall, D.P., Allison, L.C., Bigg, G.R., Donohue, K., Heywood, K.J., Hughes, C.W., Hibbert, A., Hogg, A.M., Johnson, H.L., Jullion, L., King, B.A., Leach, H., Lenn, Y.-D., Morales Maqueda, M.A., Munday, D.R., Naveira Garabato, A.C., Provost, C., Sallée, J.-B., Sprintall, J., 2011. Sustained monitoring of the Southern Ocean at Drake Passage: Past achievements and future priorities. *Rev. Geophys.* 49, 1–36. doi:10.1029/2010RG000348.1.
- Mikaloff Fletcher, S.E., Gruber, N., Jacobson, A.R., Doney, S.C., Dutkiewicz, S., Gerber, M., Follows, M., Joos, F., Lindsay, K., Menemenlis, D., Mouchet, A., Müller, S.A., Sarmiento, J.L., 2006. Inverse estimates of anthropogenic CO₂ uptake, transport, and storage by the ocean. *Global Biogeochem. Cycles* 20, GB2002. doi:10.1029/2005GB002530
- Mikaloff Fletcher, S.E., Gruber, N., Jacobson, A.R., Gloor, M., Doney, S.C., Dutkiewicz, S., Gerber, M., Follows, M., Joos, F., Lindsay, K., Menemenlis, D., Mouchet, A., Müller, S.A., Sarmiento, J.L., 2007. Inverse estimates of the oceanic sources and sinks of natural CO₂ and the implied oceanic carbon transport. *Global Biogeochem. Cycles* 21, GB1010. doi:10.1029/2006GB002751
- Mintrop, L., 2004. VINDTA, Versatile instrument for the Determination of Titration

Alkalinity., Manual for versions 3S and 3C. Version 2.0. MARine ANalytics and DATA (MARIANDA), Kiel, Germany. 45.

- Morris, M.Y., Hall, M.M., St Laurent, L.C., Hogg, N.G., 2001. Abyssal Mixing in the Brazil Basin. *J. Phys. Oceanogr.* 31, 3331–3348.
- Munk, W.H., 1966. Abyssal recipes. *Deep Sea Res.* 13, 707–730.
- Murata, A., Kumamoto, Y., Sasaki, K., Watanabe, S., Fukasawa, M., 2008. Decadal increases of anthropogenic CO₂ in the subtropical South Atlantic Ocean along 30°S. *J. Geophys. Res.* 113, C06007, doi:10.1029/2007JC004424. doi:10.1029/2007JC004424
- Naveira Garabato, A.C., Heywood, K.J., Stevens, D.P., 2002a. Modification and pathways of Southern Ocean Deep Waters in the Scotia Sea. *Deep Sea Res. Part I Oceanogr. Res. Pap.* 49, 681–705.
- Naveira Garabato, A.C., Jullion, L., Stevens, D.P., Heywood, K.J., King, B.A., 2009. Variability of Subantarctic Mode Water and Antarctic Intermediate Water in the Drake Passage during the Late-Twentieth and Early-Twenty-First Centuries. *J. Clim.* 22, 3661. doi:10.1175/2009JCLI2621.1
- Naveira Garabato, A.C., McDonagh, E.L., Stevens, D.P., Heywood, K.J., Sanders, R.J., 2002b. On the export of Antarctic Bottom Water from the Weddell Sea. *Deep Sea Res. Part II Top. Stud. Oceanogr.* 49, 4715–4742.
- Naveira Garabato, A.C., Polzin, K.L., King, B.A., Heywood, K.J., Visbeck, M., 2004. Widespread intense turbulent mixing in the Southern Ocean. *Science.* 303, 210–3. doi:10.1126/science.1090929
- Naveira Garabato, A.C., Stevens, D.P., Heywood, K.J., 2003. Water mass conversion, fluxes, and mixing in the Scotia Sea diagnosed by an inverse model. *J. Phys. Oceanogr.* 33, 2565–2587.
- Naveira Garabato, A.C., Williams, A.P., Bacon, S., 2014. The three-dimensional overturning circulation of the Southern Ocean during the WOCE era. *Prog. Oceanogr.* 120, 41–78. doi:10.1016/j.pocean.2013.07.018
- Ohshima, K.I., Fukamachi, Y., Williams, G.D., Nihashi, S., Roquet, F., Kitade, Y., Tamura, T., Hirano, D., Herraiz-Borreguero, L., Field, I., Hindell, M., Aoki, S., Wakatsuchi, M., 2013. Antarctic Bottom Water production by intense sea-ice formation in the Cape Darnley polynya. *Nat. Geosci.* 6, 235–240. doi:10.1038/ngeo1738
- Olsen, A., Key, R.M., van Heuven, S., Lauvset, S.K., Velo, A., Lin, X., Schirnick, C., Kozyr, A., Tanhua, T., Hoppema, M., Jutterström, S., Steinfeldt, R., Jeansson, E., Ishii, M., Perez, F.F., Suzuki, T., 2016. An internally consistent data product for the world ocean: the Global Ocean Data Analysis Project, version 2 (GLODAPv2). *Earth Syst. Sci. Data Discuss.* doi:10.5194/essd-2015-42
- Orsi, A.H., Johnson, G.C., Bullister, J.L., 1999. Circulation, mixing, and production of Antarctic Bottom Water. *Prog. Oceanogr.* 43, 55–109.

- Orsi, A.H., Whitworth, T., Nowlin, W.D., 1995. On the meridional extent and fronts of the Antarctic Circumpolar Current. *Deep Sea Res. Part I Oceanogr. Res. Pap.* 42, 641–673.
- Pardo, P.C., Vázquez-Rodríguez, M., Pérez, F.F., Ríos, A.F., 2011. CO₂ air–sea disequilibrium and preformed alkalinity in the Pacific and Indian oceans calculated from subsurface layer data. *J. Mar. Syst.* 84, 67–77.
doi:10.1016/j.jmarsys.2010.08.006
- Park, Y.-H., Charriaud, E., Craneguy, P., Kartavtseff, A., 2001. Fronts, transport, and Weddell Gyre at 30°E between Africa and Antarctica. *J. Geophys. Res.* 106, 2857–2879.
- Peacock, S., 2004. Debate over the ocean bomb radiocarbon sink: Closing the gap. *Global Biogeochem. Cycles* 18, GB2022, doi:10.1029/2003GB002211.
doi:10.1029/2003GB002211
- Peng, T.-H., Wanninkhof, R., 2010. Increase in anthropogenic CO₂ in the Atlantic Ocean in the last two decades. *Deep Sea Res. Part I Oceanogr. Res. Pap.* 57, 755–770.
doi:10.1016/j.dsr.2010.03.008
- Pérez, F.F., Vázquez-Rodríguez, M., Louarn, E., Padín, X.A., Mercier, H., Ríos, A.F., 2008. Temporal variability of the anthropogenic CO₂ storage in the Irminger Sea. *Biogeosciences* 5, 1669–1679.
- Peterson, R.G., Stramma, L., 1991. Upper-level circulation in the South Atlantic Ocean. *Prog. Oceanogr.* 26, 1–73.
- Piecuch, C.G., Ponte, R.M., 2012. Importance of Circulation Changes to Atlantic Heat Storage Rates on Seasonal and Interannual Time Scales. *J. Clim.* 25, 350–362.
doi:10.1175/JCLI-D-11-00123.1
- Richardson, P.L., 2007. Agulhas leakage into the Atlantic estimated with subsurface floats and surface drifters. *Deep Sea Res. Part I Oceanogr. Res. Pap.* 54, 1361–1389.
doi:10.1016/j.dsr.2007.04.010
- Rignot, E., Bamber, J.L., van den Broeke, M.R., Davis, C., Li, Y., van de Berg, W.J., van Meijgaard, E., 2008. Recent Antarctic ice mass loss from radar interferometry and regional climate modelling. *Nat. Geosci.* 1, 106–110. doi:10.1038/geo102
- Rintoul, S.R., 1991. South Atlantic Interbasin Exchange. *J. Geophys. Res.* 96, 2675–2692.
- Ríos, A.F., Velo, A., Pardo, P.C., Hoppema, M., Pérez, F.F., 2012. An update of anthropogenic CO₂ storage rates in the western South Atlantic basin and the role of Antarctic Bottom Water. *J. Mar. Syst.* 94, 197–203.
doi:10.1016/j.jmarsys.2011.11.023
- Rosón, G., Ríos, A.F., Pérez, F.F., Lavín, A., Bryden, H.L., 2003. Carbon distribution, fluxes, and budgets in the subtropical North Atlantic Ocean (24.5°N). *J. Geophys. Res.* 108, 3144. doi:10.1029/1999JC000047
- Sabine, C.L., Feely, R.A., Gruber, N., Key, R.M., Lee, K., Bullister, J.L., Wong, C.S.,

- Wanninkhof, R., Wallace, D.W.R., Tilbrook, B., Millero, F.J., Peng, T.-H., Kozyr, A., Ono, T., Rios, A.F., 2004. The oceanic sink for anthropogenic CO₂. *Science* 305, 367–71. doi:10.1126/science.1097403
- Sabine, C.L., Feely, R.A., Key, R.M., Bullister, J.L., Millero, F.J., Lee, K., Peng, T.-H., Tilbrook, B., Ono, T., Wong, C.S., 2002. Distribution of anthropogenic CO₂ in the Pacific Ocean. *Global Biogeochem. Cycles* 16, GB1083, doi:10.1029/2001GB001639. doi:10.1029/2001GB001639
- Sabine, C.L., Key, R.M., Johnson, K.M., Millero, F.J., Poisson, A., Sarmiento, J.L., Wallace, D.W.R., Winn, C.D., 1999. Anthropogenic CO₂ inventory of the Indian Ocean. *Global Biogeochem. Cycles* 13, 179–198.
- Sallée, J.-B., Matear, R.J., Rintoul, S.R., Lenton, A., 2012. Localized subduction of anthropogenic carbon dioxide in the Southern Hemisphere oceans. *Nat. Geosci.* 5, 579–584. doi:10.1038/ngeo1523
- Sarmiento, J.L., Murnane, R., Le Quéré, C., 1995. Air-sea CO₂ transfer and the carbon budget of the North Atlantic. *Philos. Trans. Biol. Sci.* 348, 211–219.
- Schanze, J.J., Schmitt, R.W., Yu, L.L., 2010. The global oceanic freshwater cycle: A state-of-the-art quantification. *J. Mar. Res.* 68, 569–595. doi:10.1357/002224010794657164
- Schröder, M., Fahrbach, E., 1999. On the structure and the transport of the eastern Weddell Gyre. *Deep Sea Res. Part II Top. Stud. Oceanogr.* 46, 501–527.
- Schuster, U., McKinley, G.A., Bates, N., Chevallier, F., Doney, S.C., Fay, A.R., González-Dávila, M., Gruber, N., Jones, S., Krijnen, J., Landschützer, P., Lefèvre, N., Manizza, M., Mathis, J., Metzl, N., Olsen, A., Rios, A.F., Rödenbeck, C., Santana-Casiano, J.M., Takahashi, T., Wanninkhof, R., Watson, A.J., 2013. An assessment of the Atlantic and Arctic sea–air CO₂ fluxes, 1990–2009. *Biogeosciences* 10, 607–627. doi:10.5194/bg-10-607-2013
- Schuster, U., Watson, A.J., Bakker, D.C.E., de Boer, A.M., Jones, E.M., Lee, G.A., Legge, O., Louwse, A., Riley, J., Scally, S., 2014. Measurements of total alkalinity and inorganic dissolved carbon in the Atlantic Ocean and adjacent Southern Ocean between 2008 and 2010. *Earth Syst. Sci. Data* 6, 175–183.
- Signorini, S.R., 1978. On the circulation and the volume transport of the Brazil Current between the Cape of São Tomé and Guanabara Bay. *Deep Sea Res.* 25, 481–490.
- Sloyan, B.M., Rintoul, S.R., 2000. Estimates of Area-Averaged Diapycnal Fluxes from Basin-Scale Budgets. *J. Phys. Oceanogr.* 30, 2320–2341.
- Sloyan, B.M., Rintoul, S.R., 2001a. Circulation, Renewal, and Modification of Antarctic Mode and Intermediate Water. *J. Phys. Oceanogr.* 31, 1005–1030. doi:10.1175/1520-0485(2001)031<1005:CRAMOA>2.0.CO;2
- Sloyan, B.M., Rintoul, S.R., 2001b. The Southern Ocean Limb of the Global Deep Overturning Circulation. *J. Phys. Oceanogr.* 31, 143–173. doi:10.1175/1520-0485(2001)031<0143:TSOLOT>2.0.CO;2

- Smethie, W.M., Weatherly, G., 1994. A15/AR15 Cruise Report: RV Knorr, 316N142_3, Tech. Rep., cchdo.ucsd.edu/data/9903/a15do.pdf.
- Smythe-Wright, D., Chapman, P., Rae, C.D., Shannon, L.V., Boswell, S.M., 1998. Characteristics of the South Atlantic subtropical frontal zone between 15°W and 5°E. *Deep Sea Res. Part I Oceanogr. Res. Pap.* 45, 167–192. doi:10.1016/S0967-0637(97)00068-X
- Speer, K., Tziperman, E., 1992. Rates of Water Mass Formation in the North Atlantic Ocean. *J. Phys. Oceanogr.* 22, 93–104.
- Speer, K., Zenk, W., Siedler, G., Pätzold, J., Heidland, C., 1992. First resolution of flow through the Hunter Channel in the South Atlantic. *Earth Planet. Sci. Lett.* 113, 287–292. doi:10.1016/0012-821X(92)90226-L
- Speer, K.G., Dittmar, T., 2008. I06S Cruise Report: RV Revelle, 33RR20080204, Tech. Rep., cchdo.ucsd.edu/data/268/i06s_33RR20080204do.pdf.
- Stoll, M.H.C., van Aken, H.M., de Baar, H.J.W., de Boer, C.J., 1996. Meridional carbon dioxide transport in the northern North Atlantic. *Mar. Chem.* 55, 205–216. doi:10.1016/S0304-4203(96)00057-6
- Stramma, L., 1989. The Brazil Current transport south of 23°S. *Deep Sea Res. Part A. Oceanogr. Res. Pap.* 36, 639–646. doi:10.1016/0198-0149(89)90012-5
- Stramma, L., Peterson, R.G., 1990. The South Atlantic Current. *J. Phys. Oceanogr.* 20, 846–859. doi:10.1175/1520-0485(1990)020<0846:TSAC>2.0.CO;2
- Sverdrup, H.U., 1940. Hydrology: British, Australian, New Zealand Antarctic Research Expedition 1929-31, Series A, 3(2) 88–126.
- Talley, L.D., Tsuchiya, M., Orr, J.C., 1989. A16C Cruise Report: RV Melville, 318HYDROS_4, Tech. Rep., cchdo.uscd.edu/data/6917/a16cdo.txt.
- Tanhua, T., Körtzinger, A., Friis, K., Waugh, D.W., Wallace, D.W.R., 2007. An estimate of anthropogenic CO₂ inventory from decadal changes in oceanic carbon content. *Proc. Natl. Acad. Sci. U. S. A.* 104, 3037–42. doi:10.1073/pnas.0606574104
- Tanhua, T., van Heuven, S., Key, R.M., Velo, A., Olsen, A., Schirnack, C., 2010. Quality control procedures and methods of the CARINA database. *Earth Syst. Sci. Data* 2, 35–49.
- Tillinger, D., Gordon, A.L., 2010. Transport weighted temperature and internal energy transport of the Indonesian throughflow. *Dyn. Atmos. Ocean.* 50, 224–232. doi:10.1016/j.dynatmoce.2010.01.002
- Tréguer, P.J., De La Rocha, C.L., 2013. The World Ocean Silica Cycle. *Ann. Rev. Mar. Sci.* 5, 477–501. doi:10.1146/annurev-marine-121211-172346
- Tsubouchi, T., Bacon, S., Naveira Garabato, A.C., Aksenov, Y., Laxon, S.W., Fahrbach, E., Beszczynska-Moller, A., Hansen, E., Lee, C.M., Ingvaldsen, R.B., 2012. The Arctic Ocean in summer: boundary fluxes and water mass transformations. *J. Geophys. Res.* 117, C01024, doi:10.1029/2011JC007174.

- Tziperman, E., Speer, K., 1994. A study of water mass transformation in the Mediterranean Sea : analysis of climatological data and a simple three-box model. *Dyn. Atmos. Ocean.* 21, 53–82.
- van Heuven, S., Hoppema, M., Huhn, O., Slagter, H., de Baar, H., 2011. Direct observation of increasing CO₂ in the Weddell Gyre along the Prime Meridian during 1973–2008. *Deep Sea Res. Part II Top. Stud. Oceanogr.* 58, 2613–2635. doi:10.1016/j.dsr2.2011.08.007
- van Heuven, S.M.A.C., 2013. Determination of the rate of oceanic storage of anthropogenic CO₂ from measurements in the ocean interior: the South Atlantic Ocean. Ph.D. Thesis. University of Groningen, 268 pp. <http://hdl.handle.net/11370/7ca23a85-1ab6-4827-b273-0d75d0cdf53a>.
- Vázquez-Rodríguez, M., Padin, X.A., Pardo, P.C., Ríos, A.F., Pérez, F.F., 2012. The subsurface layer reference to calculate preformed alkalinity and air–sea CO₂ disequilibrium in the Atlantic Ocean. *J. Mar. Syst.* 94, 52–63. doi:10.1016/j.jmarsys.2011.10.008
- Vázquez-Rodríguez, M., Touratier, F., Lo Monaco, C., Waugh, D.W., Padin, X.A., Bellerby, R.G.J., Goyet, C., Metzl, N., Ríos, A.F., Pérez, F.F., 2009. Anthropogenic carbon distributions in the Atlantic Ocean: data-based estimates from the Arctic to the Antarctic. *Biogeosciences* 6, 439–451. doi:10.5194/bg-6-439-2009
- Wang, Q., Danilov, S., Fahrbach, E., Schröter, J., Jung, T., 2012. On the impact of wind forcing on the seasonal variability of Weddell Sea Bottom Water transport. *Geophys. Res. Lett.* 39, L06603, doi:10.1029/2012GL051198. doi:10.1029/2012GL051198
- Wanninkhof, R., Dickson, A.G., Carlson, C.A., 2009. Carbon Dioxide, Hydrographic, and Chemical Data Obtained During the R/V Roger Revelle Cruise in the Indian Ocean on CLIVAR Repeat Hydrography Sections I06S_2008 (Feb. 04 - Mar. 17, 2008). http://cdiac.ornl.gov/ftp/oceans/CLIVAR/I06S_2008.data/.
- Wanninkhof, R., Doney, S.C., Bullister, J.L., Levine, N.M., Warner, M., Gruber, N., 2010. Detecting anthropogenic CO₂ changes in the interior Atlantic Ocean between 1989 and 2005. *J. Geophys. Res.* 115, C11028, doi:10.1029/2010JC006251. doi:10.1029/2010JC006251
- Wanninkhof, R., Park, G.-H., Takahashi, T., Sweeney, C., Feely, R., Nojiri, Y., Gruber, N., Doney, S.C., McKinley, G.A., Lenton, A., Le Quéré, C., Heinze, C., Schwinger, J., Graven, H., Khatiwala, S., 2013. Global ocean carbon uptake: magnitude, variability and trends. *Biogeosciences* 10, 1983–2000. doi:10.5194/bg-10-1983-2013
- Wanninkhof, R., Peng, T.-H., Huss, B., Sabine, C.L., Lee, K., 2003. Comparison of inorganic carbon system parameters measured in the Atlantic Ocean from 1990 to 1998 and recommended adjustments. *ORNL/CDIAC-140 Carbon Dioxide Inf. Anal. Cent.* 43.
- Warren, B.A., Speer, K.G., 1991. Deep Circulation in the Eastern South-Atlantic Ocean.

Deep Sea Res. Part A. Oceanogr. Res. Pap. 38, S281–S322.

- Weppernig, R., Schlosser, P., Khatiwala, S., Fairbanks, R.G., 1996. Isotope data from Ice Station Weddell: Implications for deep water formation in the Weddell Sea. *J. Geophys. Res.* 101, 25723. doi:10.1029/96JC01895
- Whitworth, T., Orsi, A.H., Kim, S.J., Nowlin, W.D., Locarini, R.A., 1998. Water masses and mixing near the Antarctic Slope Front, in: Jacobs, S.S., Weiss, R.F. (Eds.), *Ocean, Ice, and Atmosphere: Interactions at the Antarctic Continental Margin*, Antarctic Research Series. American Geophysical Union, Washington, D.C., pp. 1–27.
- Wilkin, J.L., Mansbridge, J. V., Godfrey, J.S., 1995. Pacific Ocean Heat Transport at 24°N in a High-Resolution Global Model. *J. Phys. Oceanogr.* 25, 2204–2214.
- Williams, A.P., 2007. *Antarctic Climate: Ocean fluxes and variability*. Ph.D. Thesis. University of Southampton, 204 pp.
- Woodgate, R.A., Aagaard, K., 2005. Revising the Bering Strait freshwater flux into the Arctic Ocean. *Geophys. Res. Lett.* 32, L02602. doi:10.1029/2004GL021747
- Yu, L., Jin, X., Weller, R.A., 2008. *Multidecade Global Flux Datasets from the Objectively Analyzed Air-sea Fluxes (OAFlux) Project*, Woods Hole Oceanography Institution, OAFlux Project Technical Report (OA-2008-01).
- Yu, L., Weller, R., 2007. Objectively Analyzed Air-Sea Heat Fluxes for the Global Ice-Free Oceans (1981-2005). *Bull. Am. Meteorol. Soc.* 88, 527–539.
- Zemba, J.C., 1991. *The Structure and Transport of the Brazil Current between 27° and 36° South*. Technology. Ph.D. Thesis. Massachusetts Institute of Technology and Woods Hole Oceanographic Institution, 160 pp.
- Zenk, W., Siedler, G., Lenz, B., Hogg, N.G., 1999. Antarctic Bottom Water Flow through the Hunter Channel. *J. Phys. Oceanogr.* 29, 2785–2801.